A Skewed perspective of the Indian rainfall-ENSO Relationship

Justin Schulte[1*], Fredrick Policielli[2], and Benjamin Zaitchik[3]

1. Science Systems and Applications, Inc.

2. NASA Goddard Space Flight Center

3. John Hopkins University

*corresponding Author: Justin Schulte (justin.a.schulte@nasa.gov)

Abstract

Wavelet coherence is a method that is commonly used in hydrology to extract scale-dependent, non-stationary relationships between time series. However, we show that the method cannot always determine why the time-domain correlation between two time series changes in time. We show that even for stationary coherence, the time-domain correlation between two time series weakens if at least one of the time series has changing skewness. To overcome this drawback, a nonlinear coherence method is proposed for quantifying the cross-correlation between nonlinear modes embedded in time series. It is shown that nonlinear coherence and auto-bicoherence spectra can provide additional insight into changing time-domain correlations. The new method is applied to the El Niño /Southern Oscillation (ENSO) and All-India rainfall (AIR), which is intricately linked to hydrological processes across the Indian sub-continent. The nonlinear coherence analysis showed that the skewness of AIR is weakly correlated with that of two ENSO time series after the 1970s, indicating that increases in ENSO skewness after the 1970s at least partially contributed to the weakening ENSO-AIR relationship in recent decades. The implication of this result is that the intensity of skewed El Niño events is likely to overestimate India drought severity, which was the case in the 1997 monsoon season, a time point when the nonlinear wavelet coherence between AIR and ENSO reached its lowest value in the 1871-2016 period. We determined that the association between the weakening ENSO-AIR relationship and ENSO nonlinearity could reflect the contribution of different nonlinear ENSO modes to ENSO diversity.

1. Introduction

The South Asian Monsoon, which is the dominant precipitation source for the Indian subcontinent, has been a target for seasonal prediction for well over a century (Blanford, 1884). Despite this long heritage of research, skillful prediction remains a challenge, driving extensive and ongoing research on statistically and dynamically based prediction methods (e.g., REFS). It is difficult to overstate the importance of the South Asian Monsoon to the well-being of citizens in India. Strong monsoon years have caused catastrophic flooding (Kale, 2012; Sanyal and Lu, 2005) and large landslides (Dortch et al., 2009), while weak monsoons have led to water shortages (Mishra et al., 2016) and crop losses (Parthasarathy et al., 1988; Prasanna, 2014) that, resulted in significant food shortages in historical times (Fagan, 2009). Thus, while the majority of monsoon forecast studies target prediction of rainfall totals, the hydrological and agricultural impacts of monsoon variability provide the most pressing motivation for the work.

Much of the research on South Asian Monsoon prediction has focused on the relationship between the El Niño/Southern Oscillation (ENSO; Walker and Bliss, 1932) and monsoon strength. During El Niño years, droughts are favored, while rainfall surpluses are favored during La Niña years (Shukla and Paolino, 1983; Kripalani and Kulkarni, 1997). However, there is no one-to-one relationship between ENSO and Indian rainfall. As a result, summer rainfall predictions based on ENSO have proven challenging. For example, the 1997/1998 El Niño event was extremely strong yet climatological Indian monsoon conditions were observed (Shen and Kimoto, 1999; Slingo and Annamalai, 2000). It is therefore important to understand why certain El Niño events are not accompanied by monsoon failures.

There are a few reasons for the challenges faced when predicting Indian rainfall using ENSO. The first reason is that the relationship between ENSO and India rainfall is non-stationary. As shown by Torrence and Webster (1999), the relationship between ENSO and India rainfall cycles between periods of high and low coherence. Kumar et al. (1999) found that the relationship between Indian rainfall and ENSO weakened in the 1970s and hypothesized that a southward shift in Walker circulation anomalies associated with ENSO events and increased Eurasian spring and

46 winter surface temperatures were responsible for the weakening relationship. Other works suggest that the changing
47 ENSO-Indian rainfall relationship was the result of the modulating influence of tropical Atlantic sea surface
48 temperatures (SSTs) and the Atlantic Multi-decadal Oscillation (Lu et al., 2006; Kucharski et al. 2007; Kucharksi et
49 al., 2009; Chen et al., 2010). In contrast, Kumar et al. (2006) and Fan et al. (2017) argued that the occurrence of
50 different ENSO flavors (Johnson, 2013) such as the Eastern Pacific and Central Pacific types could explain the ENSO-
51 Indian rainfall relationship changes. Other investigators adopted another perspective to explain changes in the ENSO-
52 Indian rainfall relationship and concluded that temporal undulations in the ENSO-Indian rainfall relationship are
53 related to statistical under-sampling and stochastic fluctuations (Gershunov et al. 2001; van Oldenborgh and Burgers,
54 2005; Delsole and Shukla, 2006; Cash et al., 2017). In a recent analysis, Yun and Timmermann (2018) showed that
55 changes in the ENSO-Indian rainfall relationship are consistent with a stochastically perturbed ENSO signal and
56 argued that changes in the ENSO-Indian monsoon relationship may not be related to external climate forcing
57 mechanisms.

58   The second reason for the ENSO-related prediction challenges is that ENSO itself is a non-stationary
59 phenomenon. Using wavelet analysis, Kestin et al. (1998) found that the interannual variability of ENSO from 1930
60 to 1960 was dominated by a 4- to 7- year periodicity, whereas from 1960 to 1990, the interannual variability was also
61 dominated by a 2- to 5- year periodicity. A wavelet power spectral analysis conducted by Torrence and Webster (1999)
62 and Schulte (2016a) showed that ENSO signal energy in the 2- to 7-year period band undulates throughout the
63 historical period and increases after the 1960s (Schulte 2016a).These changes in spectral characteristic are relevant to
64 Indian Monsoon prediction because differing spectral characteristics among predictors (e.g. ENSO) and predictands
65 (e.g. Indian rainfall) can negatively impact the predictive skill of statistical models (Jiang et al., 2020). Using a
66 wavelet-based variance transformation method, Jiang et al. (2020) demonstrated that accounting for differences in
67 spectral characteristics can improve prognostic skill. That study suggests that Indian Monsoon prediction could be
68 improved using wavelet-based methods instead of time-domain correlation and regression methods.

69   The nonlinear characteristics (e.g. skewness) of ENSO are also non-stationary and undergo interdecadal
70 changes (Wu and Hsieh, 2003). Numerous studies have reported an ENSO regime shift in the 1970s in which ENSO
71 began to evolve more nonlinearly than in previous decades (An, 2004; An and Jin 2004; An, 2009). It is a curious fact
72 that the ENSO regime shift of the 1970s coincided with the weakening ENSO-Indian rainfall relationship as
73 documented by Kumar et al. (1999). This observation begs the question as to whether nonlinear ENSO regime changes
74 are related to changes in the ENSO-Indian rainfall relationship.

75   Various mechanisms have been proposed for explaining the cause of ENSO skewness. Kang and Kug (2002)
76 suggested that the asymmetry between the magnitude of El Niño and La Niña events is related to the relative westward
77 displacement of zonal wind stress anomalies during La Niña events compared to El Niño events. Jin et al., (2003) and
78 An and Jin (2004) found that ENSO asymmetry is related to nonlinear dynamical heating (NDH), where the magnitude
79 of NDH is related to the propagation characteristics of ENSO. As shown by An and Jin (2004), NDH during strong
80 El Niño events like the 1982/1983 and 1997/1998 events tends to be stronger than that of weak El Niño events because
81 SST anomalies tend to propagate eastward. Since the late 1970s there has been a propensity for eastward propagation
82 characteristics of ENSO (Santoso et al., 2013), contrasting with the time period before the 1970s that consisted of the
83 relatively weak El Niño events of 1957/1958 and 1972/1973 (An and Jin, 2004; An, 2009). More recently, Su et al.
84 (2010) showed that vertical temperature advection may have an opposing effect on ENSO asymmetry and that the
85 asymmetry in the extreme eastern equatorial Pacific is related to meridional ocean temperature advection.

86   Previous investigators have used different metrics to quantify ENSO asymmetry. To measure the nonlinear
87 character of ENSO, An and Jin (2004) used time-domain metrics such as skewness and maximum potential intensity
88 (MPI) to quantify the skewness of SST anomalies and the skewness of individual ENSO events, respectively. An
89 (2004) applied a principal component analysis (PCA) to a 21- year moving window of tropical Pacific SST skewness
90 and found that the first PCA mode is characterized by positive skewness across the eastern equatorial Pacific and
91 negative skewness across the central equatorial Pacific. This pattern means that interdecadal changes in the
92 nonlinearity of ENSO is associated with positively skewed SST anomalies across the eastern equatorial Pacific,
93 implying that El Niño events are stronger than La Niña events. While the methods implemented in the aforementioned

94 studies provided important insights, they cannot reveal the frequency modes of ENSO that are contributing to the
95 skewness.

96   Recognizing the limitations of time-domain approaches, Timmermann (2003) conducted a bi-spectral
97 analysis of the Niño 3 anomaly time series, where a peak (f_1, f_2) in the bi-spectrum means there is statistical phase
98 dependence among oscillators with frequencies f_1, f_2, and $f_1 + f_2$. That bi-spectral analysis revealed statistically
99 significant bi-spectral power at several frequency pairs, including (0.038, 0.038), (0.028, 0.028), (0.0225, 0.0225),
100 (0.0045, 0.032), and (0.0045, 0.045) [month^{-1}]. The peaks (0.0045, 0.032), and (0.0045, 0.045) [months^{-1}] were
101 identified with the nonlinear interactions among 18-year and 2-year variability. Although the analysis provided new
102 insights, the Fourier-based analysis could not reveal how the nonlinear nature of ENSO changed with time, an
103 important property to capture given how the nonlinear characteristics of ENSO are non-stationary (Santoso et al.,
104 2013). Much like the cross-wavelet power (Maraun and Kurths, 2004) and time-domain covariance, bi-spectral power
105 is not a bounded quantity and so high bi-spectral power does not always mean strong phase dependence.

106   In this study, the deficiencies associated with the above-mentioned techniques are addressed using higher-
107 order wavelet analysis, which allows for the quantification of frequency-dependent and non-stationary nonlinearities
108 in time series (Van Millagan, 2004, Elsayad, 2006; Schulte, 2016b). More specifically, the objectives of the paper are
109 the following: 1) quantify the nonlinearity of ENSO using higher-order wavelet analysis together with recently
110 developed statistical tests; (2) Determine if different nonlinear modes of ENSO are associated with distinct SST
111 patterns; and (3) develop nonlinear wavelet coherence methods to test the hypothesis that the breakdown of the ENSO-
112 Indian rainfall relationship in recent decades is related to the shift of ENSO from a linear regime to a nonlinear one.
113 The paper is organized as follows: In Section 2, data used are described. Section 3 includes the description of the
114 implemented methodologies. Results are presented in Section 4 and concluding remarks are provided in Section 5.

115 **2. Data**

116   The variability of India rainfall from 1871-2016 was analyzed using the All-India rainfall (AIR; Parthasarathy
117 et al. 1994) time series, which was created by averaging representative rain gauges at various locations across India.
118 The full monsoon season (June-September) and the late monsoon (August-September) season were used to identify
119 possible within-season variations in the ENSO-All-India relationships. To remove the influence of the annual cycle,
120 AIR time series was converted into anomaly time series by subtracting the 1871-2016 long-term mean for each month
121 from the individual monthly values. The AIR anomaly (AIR, hereafter) time series were subsequently standardized
122 by dividing it by its 1871-2016 standard deviations. Because wavelet analysis focuses on specific frequency
123 components that are not impacted by long-term time-domain trends, no detrending of the data was performed.

124   The monthly data for the Niño 1+2, Niño 3, Niño 3.4, and Niño 4 indices (available at:
125 https://www.esrl.noaa.gov/psd/gcos_wgsp/Timeseries/Data/nino34.long.data) from 1871 to 2016 were used to
126 understand how the nonlinear characteristics of SSTs varied from one ENSO region to another. The Niño 1+2 index
127 is the average SST in the region with latitudinal boundaries 0° and 10°S and longitudinal boundaries 90°W and 80°W
128 and the Niño 3 index is the average SST in the region with latitudinal boundaries 5°N and 5°S and longitudinal
129 boundaries 150°W and 90°W. Variations in SSTs further west were described using the Niño 3.4 and Niño 4 indices,
130 where the Niño 3.4 index is defined as the average SST in the region bounded by 5°N and 5°S and 170°W and 120°W
131 and the Niño 4 index is defined as average SSTs in the region bounded by 5°N and 5°S and 160°E and 150°W. The
132 seasonal cycle was removed from these time series in the same way as it was removed from the All-India rainfall time
133 series.

134   The monthly SST data from 1871-2016 were based on the Hadley Centre Global Sea Ice and Sea Surface
135 Temperature (HadISST1; Rayner et al., 2003) The data at each grid point were converted to monthly anomalies in the
136 same way as they were computed for the ENSO and AIR time series.

137 **3. Methods**

138 **3.1 Wavelet Analysis**

139   To better diagnose changes in time series statistics associated with AIR and ENSO, we adopted a wavelet
140 analysis. For a time series, X, comprising data points $x_1, x_2, \ldots, x_N$, the continuous wavelet transform is given by

$$W_n(s) = \sqrt{\frac{\delta t}{s}} \sum_{n'=1}^{N} x_{n'} \, \psi_0 \left[(n' - n) \frac{\delta t}{s} \right] \tag{1}$$

142 where s is wavelet scale, ψ_0 is an analyzing wavelet, δt is a time step (1 month in this study), and n is time. The
143 sample wavelet power spectrum $|W_n(s)|^2$ measured the energy content of a signal at time n and scale s. The commonly
144 used Morlet wavelet with angular frequency $\omega = 6$ was used throughout this paper because it balances time and
145 frequency localization and because it is commonly used in hydrological and climate studies (Schaefli et al., 2007;
146 Zhang et al., 2007; Holman et al., 2001; Carey et al., 2013). The readers are referred to Torrence and Compo (1998)
147 and Grinsted et al. (2004) for more details about wavelet analysis.

148   Linear wavelet coherence (Table 1) was used to quantify the linear relationship between two time series as a
149 function of frequency and time. Linear wavelet coherence between two time series X and Y is given by

$$R_n^2(s) = \frac{\left| S s^{-1} W_n^{XY}(s) \right|^2}{S \left(s^{-1} |W_n^X(s)|^2 \right) S \left(s^{-1} |W_n^Y(s)|^2 \right)}, \tag{2}$$

151 where S is a smoothing operator (Grinsted et al., 2004) and $W_n^{XY}(s)$ is the cross-wavelet power spectrum. Two time
152 series are perfectly coherent ($R_n^2(s) = 1$) at s if $\phi_n^X(s) - \phi_n^Y(s) = c$ over a sufficiently long time interval, where c is
153 a constant, $\phi_n^X(s)$ is the phase associated with X, and $\phi_n^Y(s)$ is the phase associated with Y.

154   In the context of the Indian monsoon, strong coherence between rainfall and a climate pattern (e.g. ENSO)
155 at a scale s indicates shared temporal characteristics between a climate pattern and rainfall. Because theory supports a
156 causal link between ENSO and monsoon variability through changes in the Walker Circulation (Ropelewski and
157 Halpert, 1987), strong coherence means that when ENSO is in a warm (cool) phase at the scale s, negative (positive)
158 rainfall anomalies are preferred. Thus, a periodic climate forcing could create periodicities in an otherwise noisy
159 rainfall time series.

160 **3.2 Higher-order Wavelet Analysis**

161   Although the wavelet power spectrum is useful for quantifying the signal energy at a scale s and time n, it
162 cannot determine if there is a nonlinear relationship among different frequency components. In fact, the power
163 spectrum can only fully describe time series in frequency space in the case of linear systems in which the output is
164 proportional to the input (King, 1998). As ENSO is nonlinear, we adopted higher-order wavelet methods to address
165 the deficiencies of traditional wavelet methods.

166   The type of nonlinearities considered in this study were quadratic nonlinearities in which the scales s_1, s_2,
167 and s_3 satisfied the sum rule

$$\frac{1}{s_3} = \frac{1}{s_1} + \frac{1}{s_2} \tag{3}$$

169 and the wavelet phases satisfied

$$\phi_n(s_3) = \phi_n(s_1) + \phi_n(s_2). \tag{4}$$

171 These types of nonlinearities arise, for example, when a sinusoid is squared, in which case a harmonic is produced.
172 More generally, quadratic nonlinearities induce time series skewness, which was computed in this study using

$$skewness = \frac{\frac{1}{N} \sum_{i=1}^{N} (x_i - \bar{x})^3}{S}, \tag{5}$$

174 where S in the standard deviation of the time series and $\bar{x}$ is the mean of the time series. Positive (negative) skewness
175 meant that the right (left) tail of the time series distribution is longer than the left (right). In other words, positive

176 (negative) skewness meant that there was a tendency for positive (negative) time series events (i.e. anomalies) to be
177 more intense than negative (positive) ones.

178   In this paper, quadratic nonlinearities giving rise to time series skewness were quantified using local and
179 global wavelet-based auto-bicoherence methods (Schulte, 2016b). Global auto-bicoherence (Table 1) was computed
180 using the equation

$$181 \quad bi_{global}^X(s_1, s_2) = \frac{\left|B_{global}^X(s_1 s_2)\right|^2}{\left(\sum_{n=1}^N |W_n^X(s_1)W_n^X(s_2)|^2\right)\left(\sum_{n=1}^N |W_n^X(s_3)|^2\right)}, \tag{6}$$

182 where

$$183 \quad B_{global}^X(s_1, s_2) = \sum_{n=1}^N \widehat{W}_n^X(s_3)W_n^X(s_1)W_n^X(s_2) \tag{7}$$

184 is the global bi-spectrum and the hat denotes the complex conjugate. Identical to wavelet coherence, auto-bicoherence
185 is bounded by 0 and 1, a value of 1 indicating the strongest possible phase coupling among the phases $\phi_n(s_3)$, $\phi_n(s_2)$,
186 and $\phi_n(s_1)$ such that sum rules Eq. (3-4) is satisfied. A peak in the auto-coherence spectrum at (s_1, s_2) indicated that
187 there was quadratic phase coupling among oscillatory modes with scales s_1, s_2, and s_3 was contributing to time series
188 skewness. It is important to note that the auto-bicoherence method cannot detect other types of nonlinearities such as
189 cubic nonlinearities whose detection would require trisepctra (Collis et al., 1998).

190   To determine if the strength of the quadratic phase coupling was a function of time, the local auto-bicoherence
191 spectrum (Schulte, 2016b) given by

$$192 \quad bi_n^X(s_1, s_1) = \frac{\left|S{s_1}^{-1}B^X{}_n(s_1, s_1)\right|^2}{S\left(s_1^{-1}|W_n^X(s_1)W_n^X(s_1)|^2\right)S\left(s_1^{-1}\left|W_n^X(\frac{s_1}{2})\right|^2\right)} \tag{8}$$

193 was computed, where $B_n^X(s_1, s_1)$ is the local bi-spectrum given as

$$194 \quad B_n^X(s_1, s_1) = \widehat{W}_n^X(s_3)W_n^X(s_1)W_n^X(s_1). \tag{9}$$

195 and $s_3 = s_1/2$. In this special case, the local auto-bicoherence spectrum revealed the time-evolution of auto-
196 bicoherence estimates located along the diagonal slices of the global auto-bicoherence spectra. Local bi-phase

$$197 \quad \psi_n(s_1, s_1) = \phi_n(s_1) + \phi_n(s_1) - \phi_n(s_3) \tag{10}$$

198 was used to measure the skewness and asymmetries of waveforms. A bi-phase of 0° meant that the relationship among
199 the scale components produced positive skewness with respect to a horizonal axis so that positive deviations from the
200 mean are larger than negative deviations from the mean (King, 1998; Maccarone, 2014; Schulte, 2016b). On the other
201 hand, a bi-phase of 180° indicated negative skewness with respect to the mean. Bi-phases near -90° or 90° indicated
202 that a time series rose (fell) more quickly than it fell (rose).

203   To be consistent with the wavelet power and coherence analyses, results for the higher-order wavelet analysis
204 were casted in terms of Fourier period rather than wavelet scale. The Fourier period corresponding to s_i was denoted
205 by p_i, where the Fourier period is obtained by multiplying s_i by 1.03 for the Morlet wavelet (Torrence and Compo,
206 1998). Thus, the local diagonal slice of the auto-bicoherence spectra were plotted using the Fourier period p_1
207 corresponding to s_1 as the vertical axis and time as the horizontal axis.

3.3 Statistical Hypothesis Testing

209   The statistical significance of all wavelet spectra was evaluated using the cumulative area-wise test (Schulte,
210 2016a; Schulte, 2019) to account for the simultaneous testing of multiple hypotheses (Maraun and Kurths, 2004;
211 Maraun et al., 2014). This test evaluated the statistical significance of points in the wavelet domain based on the area
212 of contiguous regions of point-wise significance (i.e. patches) to which they belong so that larger area implies greater
213 statistical significance. Given that patch area can change as the point-wise significance changes, the cumulative area-
214 wise test was used to evaluate significance based on patch area averaged across a set of point-wise significance levels

215 (Schulte, 2019). The test was applied at the 5% cumulative area-wise significance level using point-wise significance
216 levels ranging from 0.02 to 0.18 because this choice of point-wise significance levels was shown to result in the
217 cumulative area-wise test outperforming the point-wise test in terms of true positive detection for moderate to high
218 signal-to-noise ratios even though the cumulative area-wise test is more stringent. The test was performed using the
219 Advanced Biwavelet Wavelet R software Package (available at: http://justinschulte.com/wavelets/advbiwavelet.html).
220 Technical details of the testing procedure can be found in Schulte (2019) and Appendix A.

221   To assess the statistical significance of the global auto-bicoherence estimates, a modified version of the
222 cumulative area-wise test was applied. In the modified version of the cumulative area-wise test, the normalized area
223 of patches was computed by dividing patch area by the product $\widehat{s_1}\widehat{s_2}$, where $\widehat{s_1}$ is the mean first-coordinate of the patch
224 and $\widehat{s_2}$ is the mean second coordinate. The reason for this modified normalized area is that dividing area by say, $\widehat{s_1}^2$,
225 retained the correlation between normalized area and s_2. The test was applied using the same point-wise significance
226 levels that were used to assess the statistical significance of wavelet power and coherence.

227 **3.4 Higher-order Coherence**

228   Although wavelet coherence spectra can provide information regarding how the relationship between two
229 climate variables changes at a scale s, it cannot completely explain why the time-domain correlation between the
230 climate variables temporally fluctuates. The reason is that linear wavelet coherence only examines how well the
231 variance of one time series corresponds to the variance of another at a scale s (Table 1) because linear coherence is
232 determined by the wavelet power spectra of the time series. However, for two time series to be perfectly correlated in
233 the time domain, higher skewness of one climate variable must also correspond to higher skewness of the other climate
234 variable.

235   Recognizing that skewness is important for better understanding time-domain correlation changes, the
236 quantity

237
$$Bi_n^2(s_1, s_2) = \frac{\left|Ss_{smooth}^{-1}B_n^{XY}(s_1,s_2)\right|^2}{S\left(s_{smooth}^{-1}\left|B_n^X(s_1,s_2)\right|^2\right)S\left(s_{smoth}^{-1}\left|B_n^Y(s_1,s_2)\right|^2\right)},$$
(11)

238 called third-order coherence (nonlinear coherence, hereafter) was used to determine if changes in the skewness of X
239 are associated with changes in the skewness of Y (see Appendix B for a more general definition). In Eq, (11), s_{smooth}
240 is one of the three scales, and $B_n^{XY}(s_1, s_2)$ is the third-order cross-wavelet power spectrum, which is the product of the
241 bi-spectrum of X and the conjugate of the bi-spectrum of Y, the higher-order analog of the cross-wavelet power
242 spectrum. The word cross-bispectrum was not used to avoid confusion with cross-bicoherence analysis (Van
243 Milligen,1995). Like wavelet coherence, the nonlinear coherence is bounded by 0 and 1, a value of 1 indicating that
244 the bi-spectra of X and Y at (s_1, s_2) are perfectly and linearly correlated. The statistical significance of nonlinear
245 coherence was assessed using the cumulative area-wise test in the same way as it was used to assess the statistical
246 significance of linear wavelet coherence.

247   Higher-order wavelet analysis can also be interpreted in terms of linear and nonlinear modes. A linear mode
248 $\gamma_{s_i}^X$ is the signal component of X at the scale s_i obtained by setting all wavelet coefficients to zero except those at s_i
249 and taking the inverse wavelet transform of the result. Because linear modes are only composed of a single frequency
250 component, the local cross-correlation (coherence) between $\gamma_{s_i}^X$ and $\gamma_{s_i}^Y$ is only impacted by the variances of X and Y
251 at s_i. On the other hand, nonlinear coherence measures the local cross-correlation between the skewness of $\gamma_{s_1}^X + \gamma_{s_2}^X +$
252 $\gamma_{s_3}^X$ and $\gamma_{s_1}^Y + \gamma_{s_2}^Y + \gamma_{s_3}^Y$ or between $\gamma_{s_1}^X + \gamma_{s_1/2}^X$ and $\gamma_{s_1}^Y + \gamma_{s_1/2}^Y$ in the case that $s_1 = s_2$.

253   To better understand nonlinear coherence, we supposed that

254
$$\phi_n^X(s_1) - \phi_n^Y(s_1) = c_1$$
(12)

255
$$\phi_n^X(s_2) - \phi_n^Y(s_2) = c_2$$
(13)

256
$$\phi_n^X(s_3) - \phi_n^Y(s_3) = c_3$$
(14)

257   for constants c_1, c_2, and c_3. Adding Eqs. (12) and (13) and subtracting Eq. (14) from the result produced the equality

258
$$\phi_n^X(s_1) + \phi_n^X(s_2) - \phi_n^X(s_3) - (\phi_n^Y(s_1) + \phi_n^Y(s_2) - \phi_n^Y(s_3)) =$$

259
$$\psi_n^X(s_1, s_2) - \psi_n^Y(s_1, s_2) = \psi_n^{bi}(s_1, s_2) = K , \qquad (15)$$

260   for some constant $K = c_1 + c_2 - c_3$. Thus, if X was found to be perfectly nonlinear coherent with Y, then X and Y were
261   perfectly coherent at the three scales participating in the quadratic phase coupling. Even if the coherence was perfect
262   at two scales, the relative bi-phase $\psi_n^{bi}(s_1, s_2)$ fluctuated randomly if the relative phase difference at the remaining
263   scale fluctuated randomly so that the nonlinear coherence was low. Thus, if nonlinear coherence was high, then there
264   was some non-random relationship between X and Y at all three scales even if high linear coherence was not identified
265   at one or more scales. This theoretical idea indicates that nonlinear coherence can uncover relationships that linear
266   coherence cannot (see Figure S1 in supplementary material).

267   The relative bi-phase difference $\psi_n^{bi}(s_1, s_2)$ is the higher-order analog of the relative phase difference
268   between two time series. It measures how much the cycle geometry of one time series lags that of another. A lagged
269   bi-phase of 180° means that the skewness or asymmetry of the forcing time series is opposite to that of the response.
270   For example, if the forcing has positive skewness, then the response will have negative skewness. If the relative bi-
271   phase is 0°, then negative (positive) skewness of the forcing produces negative (positive) skewness of the response,
272   contributing to the positive time-domain correlation between the time series. Scales and time points for which
273   nonlinear coherence is high are where the relative bi-phase is stable.

274   In this paper, we focused on nonlinear coherence computed along the diagonal slices ($p_1 = p_2$) of the time
275   series bi-spectras so that $s_{smooth} = s_1 = s_2$ in this study. The nonlinear coherence spectra was then plotted using p_1 as
276   the vertical axis and time as the horizonal axis. High nonlinear coherence at p_1 and n meant that the skewness or
277   asymmetry between $\gamma_{p_1}^X + \gamma_{p_1/2}^X$ and $\gamma_{p_1}^Y + \gamma_{p_1/2}^Y$ were locally cross-correlated.

278   To demonstrate the concept of nonlinear coherence, we considered a simple example in which the nonlinear
279   climate forcing time series was given by

280
$$F(t) = \cos(\frac{2\pi}{p_1} t + \varphi) + \gamma(t) \cos(\frac{2\pi}{p_3} t + 2\varphi) + W_F(t) \qquad (16)$$

281   and the response to the forcing was given as

282
$$R(t) = \cos(\frac{2\pi}{p_1} t + \varphi) + W_R(t), \qquad (17)$$

283   In Eq. (16) and Eq. (17), $\gamma(t)$ is a time-varying nonlinear coefficient, $W_F(t)$ is Gaussian white noise associated with
284   the forcing, $W_R(t)$ is Gaussian white noise associated with the response, $\varphi = 0$ is phase, and $p_1 = 2p_3 = 32$. The
285   nonlinear coefficient was assumed to be a linear function of time, i.e.,

286
$$\gamma(t) = t/500. \qquad (18)$$

287   The effect of the coefficient was to linearly increase the variance of $F(t)$ at $p_3 = 16$ and increase the strength of the
288   quadratic phase coupling between the modes with periods $p_3 = p_1/2 = 16$ and $p_1 = 32$.

289   As shown in Figure 1a, $F(t)$ (black curve) and $R(t)$ (thick green curve) evolve coherently from $t = 0$ to $t =
290   200$. After $t = 200$, $F(t)$ begins to noticeably exceed $R(t)$ at certain time points (e.g. $t = 430$) while the relationship
291   between them at other points is reversed (e.g. $t = 450$) in the sense that a positive forcing produces a negative response.
292   As a result, the correlation between $F(t)$ and $R(t)$ weakens (Figure 1b). An inspection of the wavelet coherence
293   spectrum (Figure 2a) reveals that the coherence at $p_1 = 32$ is strong and stable so that changes in the relationship
294   strength at that time scale is not the cause of the weakening time-domain correlation. The coherence at all other periods
295   is also stationary by construction so that it is not the changing relationship strength at any time scale that is causing
296   the time-domain correlation weakening. However, the variance of $F(t)$ at $p_3 = 16$ increases with time (not shown) and
297   the coherence between $F(t)$ and $R(t)$ is also weak at that time scale, implying that larger fluctuations in $F(t)$ at $p_3 = 16$
298   are not accompanied by larger fluctuations in $R(t)$. Thus, variance increase of $F(t)$ is one reason for the weakening

299   time-domain correlation, though the linear coherence and wavelet power methods cannot explain why the skewness
300   of $F(t)$ increases without a corresponding increase in the skewness of $R(t)$ (Figure 1c).

301   An inspection of the local auto-bicoherence spectrum of $F(t)$ (Figure 2b) reveals that the auto-bicoherence at
302     $p_1 = 32$ is increasing with time, indicating that the phase coupling between modes with periods $p_3 = 16$ and $p_1 = 32$
303   is strengthening with time. The bi-phase of $0°$, as indicated by arrows pointing to the right, confirms that the quadratic
304   phase coupling is contributing to the positive skewness seen in Figure 1a to an increasing degree. Furthermore, the
305   nonlinear coherence between $R(t)$ and $F(t)$ is weak and mostly statistically insignificant at $p_3 = 32$ (Figure 2c),
306   implying the skewness of $\gamma_{16}^F + \gamma_{32}^F$ is uncorrelated with the skewness of $\gamma_{16}^R + \gamma_{32}^R$, where $\gamma_{16}^F + \gamma_{32}^F$ is the sum of the
307   cosines in Eq. (16) and the components of $W_F(t)$ at $p_3 = 16$ and $p_1 = 32$. The nonlinear mode $\gamma_{16}^R + \gamma_{32}^R$ is the sum of
308   the cosine in Eq. (17) and the components of $W_R(t)$ at $p_3 = 16$ and $p_1 = 32$. Thus, the skewness of $R(t)$ in the time-
309   domain is practically uncorrelated with the skewness of $F(t)$ because the skewness of $F(t)$ is solely related to the phase
310   coupling between the modes with periods $p_3 = 16$ and $p_1 = 32$ Thus, the increase in skewness of $F(t)$ also contributes
311   to the weakening time-domain correlation.

312   The lack of nonlinear coherence at time scales for which $F(t)$ is nonlinear has implications for empirical
313   prediction. At time points when $F(t)$ is positively skewed, $R(t)$ is overestimated because $R(t)$ is not inheriting the
314   skewness of $F(t)$. That is, if one created a linear regression model based on the relationship between $F(t)$ and $R(t)$ from
315     $t = 0$ to $t = 200$ one would find that a forcing value of, say, 1 would produce a response close to 1. If the same model
316   was used to predict $R(t)$ at, say, $t = 430$ one would predict that the forcing with value around 2 should result in a
317   response near 2. However, because the relatively large value $F(430)$ results from skewness and $R(t)$ is uncorrelated
318   with its skewness, the response is only as strong as the part of $F(t)$ not resulting from the quadratic phase coupling.
319   The more nonlinear $F(t)$ becomes, the more $F(t)$ will overestimate $R(t)$ when $F(t)$ is positively skewed. Similarly, the
320   positive forcing produces a negative response at $t = 450$ because of skewness and not simply a change in variance.
321   Nonlinear coherence allows for the quantification and identification of these time-domain aberrations.

322   The weakening relationship shown in Figure 1b could lead a researcher studying a hydrological process to
323   believe that another direct forcing mechanism must be influencing the hydrological process. This belief could lead to
324   the applications of partial wavelet coherence (Ng, and Chan, 2012) and partial correlation analyses to identify another
325   influential forcing mechanism. However, in this case, there are no other direct forcing mechanisms; the weakening
326   time-domain relationship is solely related to how $F(t)$ transitioned from a linear regime to a nonlinear regime. This
327   theoretical result suggests that hydrological studies using wavelet coherence should also consider the nonlinearity of
328   the times series.

329   **4. Results**

330   **4.1 The ENSO and Indian Monsoon time series and their time-domain relationship**

331   The contrasting Niño 1+2 and Niño 4 indices are shown in Figure 3. For the Niño 1+2 time series (Figure
332   3a), a few recent notably intense warm events are located around 1982/1983, 1997/1998, and 2015/2016, coinciding
333   with the strongest El Niño events in recent decades (McPhaden, 1999, Hu and Fedorov, 2017; Santoso et al, 2017). A
334   few notably intense Niño 1+2 events are also seen in the 1800s, indicating that intense ENSO events are not unique
335   to recent decades. An inspection of Figure 3a also reveals that the recent intense warm Niño 1+2 events are also
336   skewed in the sense that they are stronger than the surrounding cool Niño 1+2 events. Unlike the 1982/1983 and
337   1997/1998 Niño 1+2 events, the 1982/1983 and 1997/1998 warm events for the Niño 4 time series are unremarkable.
338   (Figure 3b). Furthermore cool Niño 4 events are preferentially stronger than warm events after the 1960s, suggesting
339   an intensification of negative skewness.

340   The 20-year sliding skewness time series of the Niño 1+2 index (Figure 4) reveals enhanced skewness during
341   the 1800's, near zero skewness around the 1930's and early 1940's, and especially enhanced skewness after the 1970s
342   associated with an upward trend in skewness beginning around the 1940s. In contrast to the Niño 1+2 index, the
343   skewness of the Niño 4 index becomes more negative after the 1960s, and the magnitude of the skewness is generally
344   smaller than that of the Niño 1+2 time series. This finding suggests that the transition of the Niño 1+2 time series to a
345   nonlinear regime is more pronounced than the transition associated with the Niño 4 time series.

346   Interestingly, a 20-year sliding skewness analysis of AIR (Figure 4) reveals that the skewness of June-
347 September AIR remains close to zero until the 1990s despite the upward trend in Niño 1+2 skewness beginning in the
348 1940s (Figure 4a). Similarly, the skewness of August-September AIR does not increase to the extent that Niño 1+2
349 skewness does (Figure 4b). On the other hand, the skewness of August-September AIR could be negatively correlated
350 with the skewness of the Niño 4 index after the 1960s, consistent with how August-September AIR and the Niño 4
351 index are negatively correlated. The skewness of June-September AIR becomes more negative in the 1990s and 2000s,
352 but it is unclear if that negative skewness is related to ENSO, noise, or another climate pattern because the skewness
353 of the Niño 1+2 and Niño 4 indices do not change as abruptly. Negative June-September AIR skewness is accompanied
354 by enhanced positive skewness of the Niño 1+2 index prior to the 1940s, which is consistent with how June-September
355 AIR is negatively correlated with the Niño 1+2 index during that time period (Figures 5a).

356   The differences in skewness shown in Figure 4 suggests that the correlation between the ENSO time series
357 and AIR degrades after the 1970s, which is confirmed by the 20-year sliding correlation between June-September AIR
358 and ENSO time series (Figure 5a). The relationship with the Niño 1+2 generally weakens from the 1800's to the
359 2000s. In contrast, the June-September AIR-Niño 4 index relationship appears to have no long-term trend, resulting
360 in the Niño 4 index becoming more strongly correlated with AIR than the Niño 1+2 index after the 1970's.

361   The stronger AIR-Niño 4 index relationship compared to the AIR-Niño 1+2 index relationship after the
362 1970s is more evident in the August-September analysis (Figure 5b). An abrupt weakening of the August-September
363 AIR-Niño 1+2 index relationship occurs around the 1970's, with the relationship reversing around the 1990s. A
364 comparison of Figures 4b and Figures 5b reveals that the weakening and reversal of the relationship occurs during the
365 time period when the Niño 1+2 index is especially skewed. The difference in the magnitudes of Niño 1+2 and Niño
366 4 skewness after the 1970s could explain why the August-September AIR-Niño 1+2 index relationship weakens more
367 abruptly than the AIR-Niño 4 index relationship. Thus, a further investigation is needed to better understand the
368 temporal changes in ENSO statistics and their impact on the ENSO-AIR relationship.

369 **4.2. Wavelet Power Analysis and Coherence**

370   The wavelet power spectra associated with the Niño 1+2 and Niño 4 time series (Figure 6) reveal enhanced
371 variance in the 16- to 64-month band after 1965 for all the time series. The appearance of holes in contoured regions
372 suggests that there are oscillatory modes with nearby frequencies (Schulte, et al., 2015), though the wavelet power
373 spectra cannot determine if there is quadratic phase coupling between the oscillatory modes.

374   The linear wavelet coherence spectrum shown in Figure 7, indicates that the AIR relationship with the Niño
375 1+2 and Niño 4 indices in the 16- to 64-month period band breaks down after 1995, which is consistent with the
376 findings from the sliding correlation analysis shown in Figure 5. The relationship between AIR and these ENSO
377 indices also weakens around 1925, but this weakening does not appear in the sliding correlation analysis. Note that
378 the lack of linear coherence after 1995 coincides with the enhanced ENSO variance (Figure 6), implying that higher
379 ENSO variance need not be associated with higher AIR variance at those time scales so that changes in ENSO variance
380 could be contributing to the weakening ENSO-AIR time-domain correlation. However, ENSO skewness is also
381 enhanced during this time period (Figure 4) so that the weakening relationships may not be simply related to ENSO
382 variance. Thus, a further analysis is needed to extract information unrevealed by the linear wavelet power and
383 coherence methods.

384 **4.3 Local auto-bicoherence of ENSO**

385   Figure 8 shows that the local auto-bicoherence spectra of all ENSO time series contain statistically significant
386 local auto-bicoherence, but the spectrum of the Niño 4 index is only associated with a few statistically significant
387 regions such as the one around 2015 at a period of 32 months. For the Niño 1+2 index, there is an intensification auto-
388 bicoherence spectrum after the 1970s, which is consistent with the ENSO regime shift (Santoso et al., 2013). A
389 comparison of Figures 4 and 8 reveals that enhanced skewness coincides with stronger auto-bicoherence in the 32- to
390 64-month period, suggesting that the skewness partially arises from the stronger quadratic phase coupling among
391 oscillatory modes with periods ranging from 32 to 64 months.

To confirm that the nonlinear phase coupling identified in Figure 8 is associated with skewed waveforms, we inspected the corresponding local bi-phase spectra (not shown). It was found that the bi-phase in the 42- to 64-month period band is generally 0° so that the nonlinear phase coupling in that period band contributes to the positive skewness of the 1982/1983, 1997/1998, and 2015/2016 events.

4.4 Nonlinear Coherence between All-India Rainfall and ENSO

The results shown in Figure 9 indicate that the nonlinear wavelet coherence between AIR and the time series for the Niño 1+2 and Niño 4 indices is statistically significant in the 32- to 64-month period band mainly prior to the 1980s. The nonlinear coherence in this period band appears to peak around the 1972/1973 El Niño event, indicating that an increase in positive skewness of ENSO should tend to coincide with enhanced negative skewness of AIR around this time. However, much of the statistically nonlinear coherence is located during the time period when ENSO is more linear than it has been in recent decades (Figure 8) so that the effects of nonlinearities are small regardless of the nonlinear wavelet coherence. In contrast, the auto-bicoherence of the Niño 1+2 time series in the 32- to 64-month period band is statistically significant and high after the 1970s (Figure 8) so that the lack of nonlinear coherence after 1980s shown in Figure 9 is expected to impact the time-domain correlation more strongly, much like the theoretical situation shown in Figures 1 and 2. Our results are consistent with this theoretical idea because the AIR-Niño 1+2 relationship weakens more than the AIR-Niño 4 relationship after the 1970s (Figure 5), which is expected because the Nino 1+2 index is more nonlinear than the Nino 4 index during this time period. However, unlike the theoretical example shown in Figure 2, the linear coherence between the ENSO time series and AIR also weakens around the 1990s (Figure 7) so that the weakening relationship could be the result of a combination of factors that includes ENSO nonlinearity.

The 20-year sliding mean of the ENSO auto-bicoherence, coherence, and nonlinear coherence averaged in the 32 to 64-month period band further highlights the impact of ENSO nonlinearity. As shown in Figure 10a, the sliding mean nonlinear coherence between the Niño 1+2 index and AIR fluctuates less than linear coherence and reaches a clear global maximum around the 1970s before rapidly declining to a global minimum around the late 1990s when the Niño 1+2 index is very nonlinear. As shown in Figure 10a, the Niño 1+2 auto-bicoherence peaks around the same time that the August-September AIR-Niño 1+2 index correlation is positive. In fact, the correlation between the sliding September-August AIR-Niño 1+2- correlation time series and the sliding Niño 1+2 auto-bicoherence time series is 0.81, much higher than the correlation with the linear coherence ($r = -0.11$) and nonlinear coherence ($r = -0.34$) time series. These results support the idea that the Niño 1+2 regime shift impacted the weakening time-domain correlation. On the other hand, the correlation between Niño 4 auto-bicoherence and the August-September AIR-Niño 4 correlation time series is weak so that changes in the nonlinearity of the Niño 4 index unlikely contributes substantially to changes in the AIR-Niño 4 relationship. Nevertheless, this result agrees with theory that suggests that nonlinearity is only an important contributor when the timeseries is highly nonlinear, which is not the case for the Niño 4 index because of the low auto-bicoherence (Figures 8b and 10b). Because the nonlinear coherence between AIR and indices for the Niño 1+2 and Niño 4 is weak (Figures 9 and 10), the more pronounced change in the August-September AIR-Nino 1+2 correlation reflects the more intense increase in Niño 1+2 nonlinearity compared to that of the Niño 4 index in recent decades.

4.5. A possible explanation for the ENSO Nonlinearity Impacts

To better understand the association between ENSO nonlinearity and the AIR-ENSO relationship, the global auto-bicoherence spectra associated with the ENSO time series were first computed (Figure 11). Then, the auto-bicoherence of SSTs associated with a few select peaks (p_1, p_2) in Figure 8 were computed at each grid point in the domain bounded by 20°N and 20°S and by 146°E and 80°W. The peaks were selected based on the auto-bicoherence spectra of the Niño 3.4 and Niño 1+2 indices. To select the peaks, local maxima in auto-bicoherence within the statistically significance regions shown in Figure 11 were identified, where points associated with local maxima were chosen because they were associated with the clearest patterns.

The spatial structure of global auto-bicoherence corresponding to the peaks in the Niño 3.4 auto-bicoherence spectrum are shown in Figure 12. The auto-bicoherence associated with the pair (31, 31) is greatest across the central equatorial Pacific, with the overall spatial pattern being reminiscent of a central Pacific El Niño (Lee and McPhaden,

440 2010). This result suggests that the phase coupling between the 31-month mode and the 15.5-month mode could be
441 related to the occurrence of central Pacific El Niño events (Section 5). In contrast, the auto-bicoherence pattern
442 associated with the pair (56, 56) is more uniform, with auto-bicoherence slightly greater across the extreme eastern
443 equatorial Pacific than the central equatorial Pacific. This pattern is reminiscent of an eastern Pacific El Niño. Like
444 the pattern corresponding to the pair (31, 31), the auto-bicoherence for the pair (105, 57) tends to be greater across the
445 central equatorial Pacific. Our findings suggest that different nonlinear modes contribute to different ENSO flavors.
446 Although An and Jin (2004) and Burgers and Stephenson (1999) showed that skewness is greatest across the eastern
447 equatorial Pacific, we determined that such a time-domain approach is unable to capture frequency-dependent patterns
448 in nonlinearity.

449   The spatial auto-bicoherence plots associated with the peaks in the Niño 1+2 auto-bicoherence spectrum are
450 shown in Figure 13. The auto-bicoherence associated with the pairs (148, 53) and (148, 105) is strong across the
451 eastern equatorial Pacific but weak across the central equatorial Pacific, suggesting that the quadratic phase coupling
452 between the 148- and 105-month modes and between the 148- and 53-month modes are associated with the skewness
453 of eastern equatorial Pacific SSTs. The pattern associated with the pair (62, 44) is reminiscent of an eastern Pacific El
454 Niño and the auto-bicoherence associated with the pair (88, 88) is relatively weak across the entire equatorial Pacific.
455 A comparison of Figures 12 and 13 shows that there is a tendency for auto-bicoherence to be greater across the eastern
456 equatorial Pacific than the central equatorial Pacific, which is consistent with how SSTs across the eastern equatorial
457 Pacific are most skewed (Burgers and Stephenson, 1999; An and Jin, 2004).

5. Discussion/Conclusion

459   The nonlinear nature of ENSO was examined using higher-order wavelet methods. The auto-bicoherence
460 spectra of the Niño 1+2 and Niño 4 indices time series revelaed that ENSO skewness arose from the quadratic phase
461 coupling of modes with various periods. For the Niño 1+2 index, the quadratic phase coupling after the 1970s was
462 especially strong, which is consistent with how ENSO underwent a regime shift around the 1970s (Santoso et al.,
463 2013) marked by an increase in ENSO skewness. Although the Niño 3.4 time series was not considered in detail in
464 this study, an auto-bicoherence analysis of the time series (not shown) revealed phase coupling between modes with
465 periods of 31 and 15.5 months in addition to coupling between modes with periods of 61 and 30.5 months. The phase
466 coupling between the 31 and 15.5 modes was found to be especially strong after 1995, whereas the quadratic phase
467 coupling between the 61- and 30.5-month modes was found to intensify after the 1970s. These additional results
468 suggest that nonlinear modes vary in intensity and time of occurrence.

469   The evolution of SSTs across the Niño 4, Niño 3.4, Niño 3, and Niño 1+2 regions was found to be nonlinear,
470 but the degree to which the time series are nonlinear are different (Figure 11). Overall, the Niño 1+2 time series was
471 found to be the most nonlinear, while the Niño 4 index was found to be the most linear. The spatial patterns associated
472 with the nonlinearities depend on the frequency components contributing to the nonlinearities. For example, the
473 quadratic phase coupling between the modes with periods of 31 and 15.5 months was found to be strongest in the
474 central equatorial Pacific and weakest across the eastern equatorial Pacific. This finding suggest that the more frequent
475 occurrence of central Pacific El Niño events in recent decades (Lee and Mcphaden, 2010) could be linked to the
476 strengthening of this quadratic phase coupling, which could explain the relationship between ENSO nonlinearity and
477 changes in the ENSO-AIR because central Pacific El Niño events have been shown to be more effective at creating
478 drought-inducing subsidence over India (Kumar et al., 2006).

479   The results from the present and previous studies (Fan et al. 2017) supports the idea that changes in the
480 ENSO-AIR relationship are related to ENSO flavors because ENSO nonlinearity appears to be related to ENSO flavors
481 (Figures 12 and 13), opposing the findings of other work showing that the changes are related to sampling variability
482 or to noise. According to Yun and Timmermann (2018), the changes in the time-domain correlation between AIR and
483 ENSO is consistent with the assumption that AIR is the sum of the ENSO signal and Gaussian white noise (i.e., AIR
484 = ENSO + white noise). However, for this hypothesis to hold, the difference AIR – ENSO must be Gaussian white
485 noise. As shown in this study, the nonlinear wavelet coherence between ENSO metrics and AIR is weak so that ENSO
486 – AIR contains periodicities (Figure S2), which means that AIR is not simply a stochastically perturbed ENSO signal,

487   as noise does not contain periodicities. The retention of non-Gaussian noise features was certainly the case for $R(t)$ –
488    $F(t)$ in the example in Section 3.5 because the difference retains the cosine function with a period of 16.

489   The fact that nonlinear coherence between rainfall and ENSO is determined by linear coherence between
490   ENSO and rainfall at two or three frequencies means that the changing time-domain correlation could be more fully
491   understood by determining why linear coherence changes at the frequencies that contribute to ENSO skewness. Such
492   an analysis could provide a more mechanistic perspective than the theoretical perspective adopted in this study. A
493   preliminary analysis showed that enhanced linear coherence between the North Atlantic Oscillation index and AIR
494   after 1995 in the 16- to 64-month period band associated with ENSO nonlinearity. This result suggests that conditions
495   across the North Atlantic (Kakade, 2000, Bhatla, 2016) could influence the nonlinear coherence between ENSO and
496   AIR and thus the corresponding time-domain correlation.

497   The tools used and developed in this study may have important applications in understanding how forecasting
498   systems replicate Indian rainfall and its associated teleconnections. These methods, for example, could determine if
499   forecasting systems can reproduce nonlinear characteristics of climate time series. As such, a R software package has
500   been developed to implement these methods (available at: http://justinschulte.com/wavelets/advbiwavelet.html; last
501   access: 22 November 2019). These methods could provide new directions for improving current forecasting systems
502   and ultimately predictions of Indian rainfall.

503

504

505

Appendix A

506

507   The first step (STEP 1) in assessing the cumulative-area significance of a point was the calculation of the N
508 $= 12$ sets

$$P_{pw}^i = \{(b,a): \rho_{pw}(b,a) < \alpha_i\}, \tag{A1}$$

509

510 where each set is the subset of the wavelet domain consisting of points whose wavelet quantities are point-wise
511 statistically significant at the α_i significance level (i.e. the pont-wise test p-value, ρ_{pw}, is less than α_i. In this paper,
512 $\alpha_1 = 0.02$, $\alpha_{12} = 0.18$, and $\alpha_{i+1} - \alpha_i = 0.02$. In the second step (STEP 2), a geometric pathway about x was computed,
513 where a geometric pathway is a nested sequence

$$P_1^x \subseteq P_2^x \subseteq \cdots \subseteq P_N^x \tag{A2}$$

514

515 such that the

$$P_i^x = \{(b,a): (b,a) \in P_{pw}^i, (b,a) \sim x\} \tag{A3}$$

516

517 are path-components of P_{pw}^i containing x. The equivalence relation $\sim$ on P_{pw}^i makes two points in P_{pw}^i equivalent if
518 they can be connected by a continuous path in P_{pw}^i. The third step (STEP 3) involved the calculation of the normalized
519 area corresponding to P_i^x. The normalized area is defined as patch area divided by the square of mean scale coordinate
520 of the patch, where A_i^x was assumed to be 0 if $P_i^x = \phi$ or $P_i^x = \{x\}$. The critical area A_i^{crit} was obtained by computing
521 the $(1 - \alpha_c)$th percentile of the null distribution of normalized areas corresponding to the significance level α_i, where
522 α_c is the significance level of the cumulative area-wise test. The null distributions were constructed by generating
523 1000 patches at the α_i significance level under the null hypothesis of red noise. The final step (Step 4) was to compute

$$r^x = \frac{1}{N}\sum_{j=1}^{N} \lambda_j^x, \tag{A4}$$

524

525 where $\lambda_i^x = 2$ if $A_i^x/A_i^{crit} > 1$ and $\lambda_i^x = 0$ if $A_i^x/A_i^{crit} <= 1$. The wavelet quantity at the point x was deemed statistically
526 significant at the α_c cumulative area-wise level if $r^x > 1$.

527

528 **Appendix B**

529   For $p > 1$, the $(p+1)$-th order poly spectrum of a time series X is given by

530
$$B_n^X(s_1, s_2, \ldots, s_p) = \widehat{W}_n^X(s_{p+1}) \left(\prod_{k=1}^p W_n^X(s_k) \right) \tag{B1}$$

531 where

532
$$\frac{1}{s_{p+1}} = \sum_{k=1}^p \frac{1}{s_k} \tag{B2}$$

533 The third-order poly spectrum is the bi-spectrum, and the fourth-order poly spectrum is the tri-spectrum (Collis et al.,
534 1998), which identifies the frequency components contributing to kurtosis. The $(p+1)$-th order coherence between two
535 time series is given as

536
$$R_n^2(s) = \frac{\left| S s_{smoth}^{-1} B_n^{XY}(s_1, s_2, \ldots, s_p) \right|^2}{S\left(s_{smooth}^{-1} |B_n^X(s_1, s_2, \ldots, s_p)|^2 \right) S\left(s_{smooth}^{-1} |B_n^Y(s_1, s_2, \ldots, s_p)|^2 \right)}, \tag{B3}$$

537 where $B_n^{XY}(s_1, s_2, \ldots, s_p)$ is the $(p+1)$-th-order cross-spectrum given by

538
$$B_n^{XY}(s_1, s_2, \ldots, s_p) = B_n^X(s_1, s_2, \ldots, s_p) \hat{B}_n^Y(s_1, s_2, \ldots, s_p). \tag{B4}$$

539 When $p = 2$, Eq. (B3), measures the local cross-correlation between skewness, and when $p = 3$, the equation
540 measures the local cross-correlation between kurtosis.

541

542

543

544

545

546

547

548

549

550

551

552

553

554

555

556

557

558

559

560   **Data/code availability**

561   Data for Indian rainfall can be accessed through https://www.tropmet.res.in/DataArchival-51-Page (Indian Institute
562   of   Tropical   Meteorology,   2019).   The   monthly   ENSO   indices   are   available   at
563   https://www.esrl.noaa.gov/psd/gcos_wgsp/Timeseries/ (NOAA/OAR/ESRL PSD, 2019). An R software package used
564   to   implement   the   new   methods   can   be   found   on   the   author's   webpage.   (available   at:
565   http://justinschulte.com/wavelets/advbiwavelet.html; last access: 22 November 2019).

566

567

568

569

570

571

572

573

574

575

576

577

578

579

580

581

582

583

584

585

586

587

588

589

590

591

592

References

594   An, S.-I., and Jin, F.-F: Nonlinearity and asymmetry of ENSO., J. Climate, 17, 2399–2412, 2004.

595   An, S.-I., Ham, Y. G., Kug, J. S., Jin, F.-F., and Kang, I.: El Nino-La Nina asymmetry in the coupled model
596   intercomparison project simulations, J. Climate, 18, 2617-2627, 2005.

597   An, S-I.: Interdecadal changes in the El Niño-La Niña symmetry, Geophys Res. Lett., 31, L23210,
598   doi:10.1029/2004GL021699, 2004.

599   An, S.-I.: A review of interdecadal changes in the nonlinearity of the El Nino–Southern Oscillation, Theor. Appl.
600   Climatol., 97, 29–40, 2009.

601   Ashok, K., Guan, Z., and Yamagata, T.: Impact on the Indian Ocean dipole on the relationship between the Indian
602   monsoon rainfall and ENSO, Geophys Res. Lett., 28, 4499–4502, 2001.

603   Ashok, K, Guan, Z, Saji, N. H., and Yamagata, T.: Individual and combined influences of ENSO and the Indian Ocean
604   dipole on the Indian summer monsoon, J. Climate, 17, 3141–3155, 2004.

605   Bhatla, R., Singh, A. K., Mandal, B., Ghosh, S., Pandey, S. N., and Abhijit, S.: Influence of North Atlantic Oscillation
606   on Indian Summer Monsoon Rainfall in Relation to Quasi-Binneal Oscillation, Pure and Applied Geophysics, 173,
607   2959-2970, 2016.

608   Blanford, H. F.: On the connexion of the Himalaya snowfall with dry wind and seasons of drought in India, Proc R
609   Soc Lond., 37, 3–22, 1884.

610   Burgers, G., and Stephenson, D. B: The 'Normality' of ENSO, Geophys Res. Lett., 26, 1027–1030, 1999.

611   Carey, S. K., Tetzlaff, D., Buttle, J., Laudon, H., McDonnell, J,. McGuire, K., Seibert, J., Soulsby, C., Shanley, J. :
612   Use of color maps and wavelet coherence to discern seasonal and inter annual climate influences on streamflow
613   variability in northern catchments. Water Resources Research, 49, 6194–6207, 2013.

614   Cash, B. A., Barimalala, R., Kinter, J. L., Altshuler, E. L., Fennessy, M. J., Manganello, J.V., Molteni, F., Towers, P.,
615   Vitart, F.: Sampling variability and the changing ENSO–monsoon relationship, Clim. Dyn., 48, 4071–4079, 2017.

616   Chen, W., Dong, B., and Lu, R.: Impact of the Atlantic Ocean on the multidecadal fluctuation of El Niño-Southern
617   Oscillation-South Asian monsoon relationship in a Coupled General Circulation Model, Journal of Geophysical
618   Research, 115, D17109, https://doi.org/10.1029/2009JD013596, 2010.

619   Collis, W. B., White, P. R., and Hammond, J. K.: Higher-order Spectra: The Bispectrum and Trispectrum, Mech. Syst.
620   Signal Pr., 12, 375–394, 1998.

621   Dortch, J. M., Owen, L. A., Haneberg, W. C., Caffee, M. W., Dietsch, C., and Kamp, U.: Nature and timing of large
622   landslides in the Himalaya and Transhimalaya of northern India, Quaternary Science Reviews, 28, 1037-1054, 2009.

623   Duan, W., Huang, C., Xu, H.: Nonlinearity modulating intensities and spatial structures of central Pacific and eastern
624   Pacific El Niño events, Adv Atmos Sci., 34, 737–756, 2017.

625   DelSole, T., and Shukla, J.: Climate models produce skillful predictions of Indian summer monsoon rainfall, Geophys
626   Res. Lett, 39, L09703, https://doi.org/10.1029/2012GL051279, 2012.

627   Elsayed, M. A. K.: Wavelet Bicoherence Analysis of Wind–wave Interaction, Ocean Eng., 33, 458–470, 2006.

628   Fagan, B.: Floods, famines, and emperors: El Niño and the fate of civilizations, Basic Books, 2009.

629 Fan, F., Dong, X., Fang, X., Xue, F., Zheng, F., and Zhu, J.: Revisiting the relationship between the south Asian
630 summer monsoon drought and El Niño warming pattern, Atmospheric Sci. Lett., 18, 175–182, 2017.

631 Gershunov, A., Schneider, N., and Barnett, T.: Low-frequency modulation of the ENSO-Indian monsoon rainfall
632 relationship: Signal or noise?, J. Climate, 14, 2486–2492, 2001.

633 Grinsted, A., Moore, J. C., and Jevrejeva, S.: Application of the Cross Wavelet Transform and Wavelet Coherence to
634 Geophysical Time Series, Nonlinear Proc. Geophys., 11, 561–566, 2004.

635 Holman, I. P., Rivas-Casado, M., Bloomfield, J.P., Gurdak, J. J.: Identifying nonstationary groundwater level response
636 to North Atlantic ocean–atmosphere teleconnection patterns using wavelet coherence. Hydrogeol. J. http://
637 dx.doi.org/10.1007/s10040-011-0755-9, 2011.

638 Hu, S. and Fedorov, A. V.: The extreme El Nino of 2015–2016̃ and the end of global warming hiatus, Geophys. Res.
639 Lett., 4415 3816–24, 2017

640 Jiang, Z., Sharma, A., & Johnson, F. (2020). Refining Predictor Spectral Representation Using Wavelet Theory for
641 Improved   Natural   System   Modeling.   Water   Resources   Research,   56(3),   e2019WR026962.
642 doi:10.1029/2019wr026962.

643 Jin, F.-F., An, S-I., Timmermann, A., and Zhao, J.: Strong El Nino events and nonlinear dynamical heating, Geophys.
644 Res. Lett., 30, 1120, doi:10.1029/2002GL016356, 2003.

645 Johnson, N.C.: How Many ENSO Flavors Can We Distinguish?, J. Climate, 26, 4816–4827, 2013.

646 Johnson N. C., and Kosaka, Y.: The role of eastern equatorial Pacific convection on the diversity of boreal winter El
647 Niño teleconnection patterns, Clim. Dyn., 47, 3737–3765, 2016.

648 Johnson, S. J., Turner, A., Woolnough, S., Martin, G., and MacLachlan, C.: An assessment of Indian monsoon
649 seasonal forecasts and mechanisms underlying monsoon interannual variability in the Met Office GloSea5-GC2
650 system. Climate Dynamics, 48(5-6), 1447-1465, 2017.

651 Kakade, S. B., and Dugam, S. S.: The simultaneous effect of NAO and SO on the monsoon activity over India,
652 Geophys Res Lett., 27, 3501–3504, 2000.

653 Kale, V. : On the link between extreme floods and excess monsoon epochs in South Asia, Climate dynamics, 39,
654 1107-1122, 2012.

655 Kalnay, E., and Dalcher, A.: Forecasting forecast skill., Mon. Wea. Rev.,115, 349–356, 1987.

656 Kang, I.-S., and Kug, J-S.: El Nino and La Ni ~ na sea surface ~ temperature anomalies: Asymmetry characteristics
657 associated with their wind stress anomalies, J. Geophys. Res., 107, 4372, doi:10.1029/2001JD000393, 2002.

658 Kestin, T. A., Karoly, D. J., Yano, J.-I., and Rayner, N. A.: Time– frequency variability of ENSO and stochastic
659 simulations, J. Climate, 11, 2258–2272, 1998.

660 King, T.: Quantifying Nonlinearity and Geometry in Time Series of Climate, Quaternary Sci. Rev., 15, 247–266,
661 1996.

662 Kripalani, R. H., and Kulkarni, A.: Climatic impact of El Nino/La Nina on the Indian monsoon: A new
663 perspective, Weather, 52, 39-46, 1997.

664 Kucharski, F., Bracco, A., Yoo, J. H., and Molteni, F.: Low-frequency variability of the Indian monsoon–ENSO
665 relationship and the tropical Atlantic: The "weakening" of the 1980s and 1990s, J. Climate., 20, 4255–4266, 2007.

666 Kucharski, F., Bracco, A., Yoo, J. H., Tompkins, A. M., Feudale, L., Ruti, P., and Dell'Aquila, A.: A gill-Matsuno-
667 type mechanism explains the tropical Atlantic influence on African and Indian monsoon rainfall, Quarterly Journal of
668 the Royal Meteorological Society, 135, 569–579, 2009.

Kumar, K. K., Soman, M. K., and Kumar, K. R.: Seasonal forecasting of Indian summer monsoon rainfall: a review, Weather, 50, 449-467, 1995

Krishnamurthy, V., and Goswami, B. N.: Indian monsoon–ENSO relationship on interdecadal timescale, J. Climate, 13, 579–595, 2000.

Kripalani, R. H., and Kulkarni, A.: Climatic impact of El Nino/ La Nina on the Indian monsoon: A new perspective, Weather, 52, 39–46, 1997.

Kumar, K. K., Rajagopalan, B., and Cane, M. A.: On the weakening relationship between the Indian monsoon and ENSO, Science, 284, 2156–2159, 1999.

Kumar, K. K., Rajagopalan, B., Hoerling, M., Bates, G., Cane, M. A.: Unraveling the Mystery of Indian Monsoon Failure During El Niño, Science, 314, 115-119, 2006.

Lee, T., and McPhaden, M. J.: Increasing intensity of El Niño in the central-equatorial Pacific, Geophys. Res. Lett., 37, L14603, doi: 10.1029/2010GL044007, 2010.

Lu, R., Dong, B., and Ding, H.: Impact of the Atlantic Multidecadal Oscillation on the Asian summer monsoon, Geophys. Res. Lett., 33, L24701, https://doi.org/10.1029/2006GL027655, 2006.

McPhaden, M. J.: Genesis and evolution of the 1997–98 El Nino, Science, 283, 950–954, 1999.

Maccarone, T. J.: The Biphase Explained: Understanding the Asymmetries in Coupled Fourier Components of Astronomical Timeseries, Mon. Not. R. Astron. Soc., 435, 3547, doi:10.1093/mnras/stu1824, 2013.

Maraun, D.,and Kurths, J.: Cross wavelet analysis: significance testing and pitfalls. Nonlinear Process. Geophys., 11, 505–514., 2004.

Maraun, D., Kurths, J., and Holschneider, M.: Nonstationary Gaussian Processes in the Wavelet Domain: Synthesis, Estimation, and Significance Testing, Phys. Rev. E, 75, 016707, doi:10.1103/PhysRevE.75.016707, 2007.

Mishra, V., Aadhar, S., Asoka, A., Pai, S., & Kumar, R.: On the frequency of the 2015 monsoon season drought in the Indo-Gangetic Plain, Geophysical Research Letters, 43, 12-102, 2016.

Munot, A. A., and Kumar, K. K.: Long range prediction of Indian summer monsoon rainfall. Journal of earth system science, 116, 73-79, 2007.

Ng, E. K. W. and Chan, J. C. L.: Geophysical applications of partial wavelet coherence and multiple waveletcoherence, J. Atmos. Ocean. Tech., 29, 1845–1853, 2012.

Parthasarathy, B., Munot, A. A., and Kothawale, D. R.: Regression model for estimation of Indian foodgrain production from summer monsoon rainfall, Agricultural and Forest Meteorology, 42, 167-182, 1988.

Parthasarathy, B., Munot, A. A., and Kothawale, D. R.: All-India monthly and seasonal rainfall series: 1871–1993, Theoretical and Applied Climatology, 49, 217–224. 1994.

Pokhrel, S., Saha, S. K., Dhakate, A., Rahman, H., Chaudhari, H. S., Salunke, K.,Hazra, A., Sujith, K., Sikka, D. R.: Seasonal prediction of Indian summer monsoon rainfall in NCEP CFSv2: forecast and predictability error, Climate dynamics, 46, 2305-2326, 2016.

Prasanna, V. (2014). Impact of monsoon rainfall on the total foodgrain yield over India. *Journal of earth system science*, *123*(5), 1129-1145, 2014.

Rajeevan, M., Pai, D. S., Kumar, R. A., and Lal, B.: New statistical models for long-range forecasting of southwest monsoon rainfall over India, Climate Dynamics, 28, 813-828, 2007.

Rayner, N. A., Parker, D. E., Horton, E. B., Folland, C. K., Alexander, L. V., Rowell, D. P., Kent, E. C., and Kaplan, A.: Global analyses of sea surface temperature, sea ice, and night marine air temperature since the late nineteenth century, J. Geophys. Res., 108, 4407, doi: 10.1029/2002JD002670,2003.

Ropelewski, C. F, Halpert ,M. S. : Global and regional scale precipitation patterns associated with the El Niño/Southern Oscillation., Monthly Weather Review, 115, 1606–1626, 1987.

Roy, I. and Tedeschi, R. G.: Influence of ENSO on regional indian summer monsoon precipitation—local atmospheric influences or remote influence from pacific, Atmosphere, 7, 25, 2016.

Santoso, A., McGregor, S., Jin, F.-F., Cai, W., England, M. H., An, S.-I., McPhaden, M. J., and Guilyardi, E.: Late-twentieth-century emergence of the El Niño propagation asymmetry and future projections., Nature, 504, 126–130, 2013.

Santoso, A., McPhaden, M. J., Cai, W.: The defining characteristics of ENSO extremes and the strong 2015/2016 El Niño, Rev. Geophys, 55, 1079–1129, 2017.

Sanyal, J., and Lu, X. X.: Remote sensing and GIS-based flood vulnerability assessment of human settlements: a case study of Gangetic West Bengal, India. Hydrological Processes: An International Journal, 19, 3699-3716, 2005.

Schaefli, B., Maraun, D., and Holschneider, M.: What drives high flow events in the Swiss Alps? Recent developments in wavelet spectral analysis and their application to hydrology, Adv. Water Resour., 30, 2511–2525, 2007.

Schulte, J. A.: Statistical hypothesis testing in wavelet analysis: theoretical developments and applications to Indian rainfall, Nonlin. Processes Geophys., 26, 91-108, https://doi.org/10.5194/npg-26-91-2019, 2019.

Schulte, J. A.: Cumulative areawise testing in wavelet analysis and its application to geophysical time-series, Nonlin. Processes Geophys., 23, 45-57, 2016.

Schulte, J. A.: Wavelet analysis for non-stationary, nonlinear time series, Nonlin. Processes Geophys., 23, 257-267, https://doi.org/10.5194/npg-23-257-2016, 2016.

Schulte, J. A., Duffy, C., and Najjar, R. G.: Geometric and Topological Approaches to Significance Testing in Wavelet Analysis, Nonlin. Processes Geophys., 22, 139-156, 2015.

Shen, X., and Kimoto, M.: Influence of El Niño on the 1997 Indian summer monsoon, J. Meteor. Soc. Japan, 77, 1023–1037, 1999.

Shukla, J., and Paolino, D. A.: The Southern Oscillation and long-range forecasting of the summer monsoon rainfall over India. Monthly Weather Review, 111, 1830-1837, 1983.

Slingo, J. M., and Annamalai, H.: 1997: The El Niño of the century and the response of the Indian summer monsoon, Mon. Wea. Rev., 128, 1778–1797, 2000.

Timmermann, A.: Decadal ENSO amplitude modulations: A nonlinear mechanism, Global Planet. Change, 37, 135–156, 2003.

Torrence, C., and Webster, P. J.: Interdecadal changes in the ENSO-monsoon system, J. Climate, 12, 2679–2690. 1999.

Van Milligen, B. P., Saìnchez, E., Estrada, T., Hidalgo, C., Brañas,B., Carreras, B., and Garcìa, L.: Wavelet Bicoherence: A New Turbulence Analysis Tool, Phys. Plasmas, 2, 3017–3032, 1995.

Walker, G. T., and Bliss, E. W.: World weather V, Mem., R. Meteorol. Soc., 4, 53–84, 1932.

Wu, A., and Hsieh, W. W.: Nonlinear interdecadal changes of the El Niño-Southern Oscillation, Climate Dyn., 21, 719–730, 2003.

Yun, K. S and Timmermann, A.: Decadal monsoon-ENSO relationships reexamined, Geophys Res Lett., 45, 2014–2021, 2018.

Zhang, Q., Xu, C., Jiang, T., Wu, Y.: Possible influence of ENSO on annual maximum streamflow of the Yangtze River, China, Journal of Hydrol, 333, 265–274. doi:10.1016/ j.jhydrol.2006.08.010, 2007.

752

753
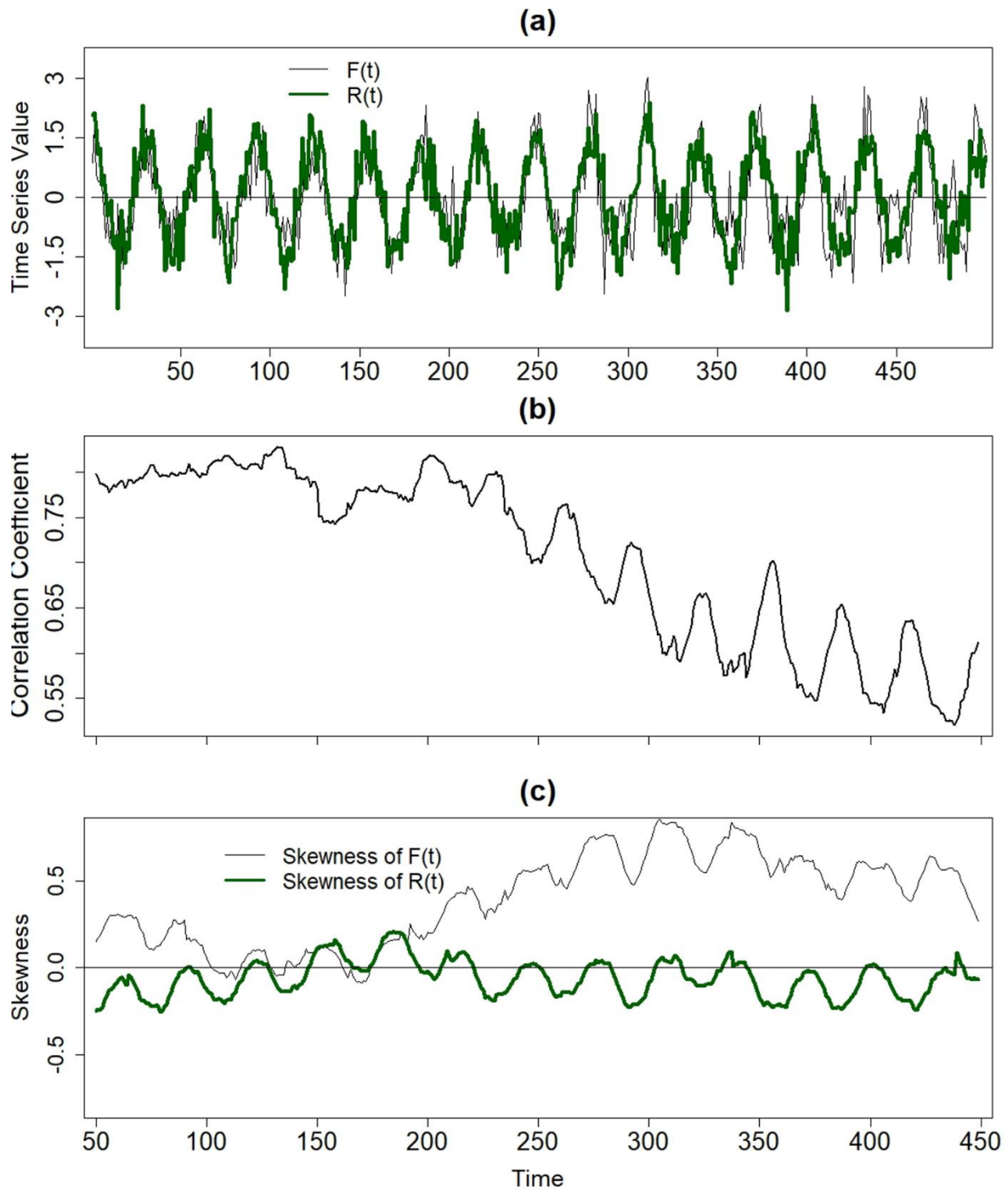
Figure 1. (a) An idealized nonlinear forcing time series together with an idealized response $R(t)$. The 120-point sliding correlation between $F(t)$ and $R(t)$. (c) The 120-point sliding skewness of $F(t)$ and $R(t)$.

756
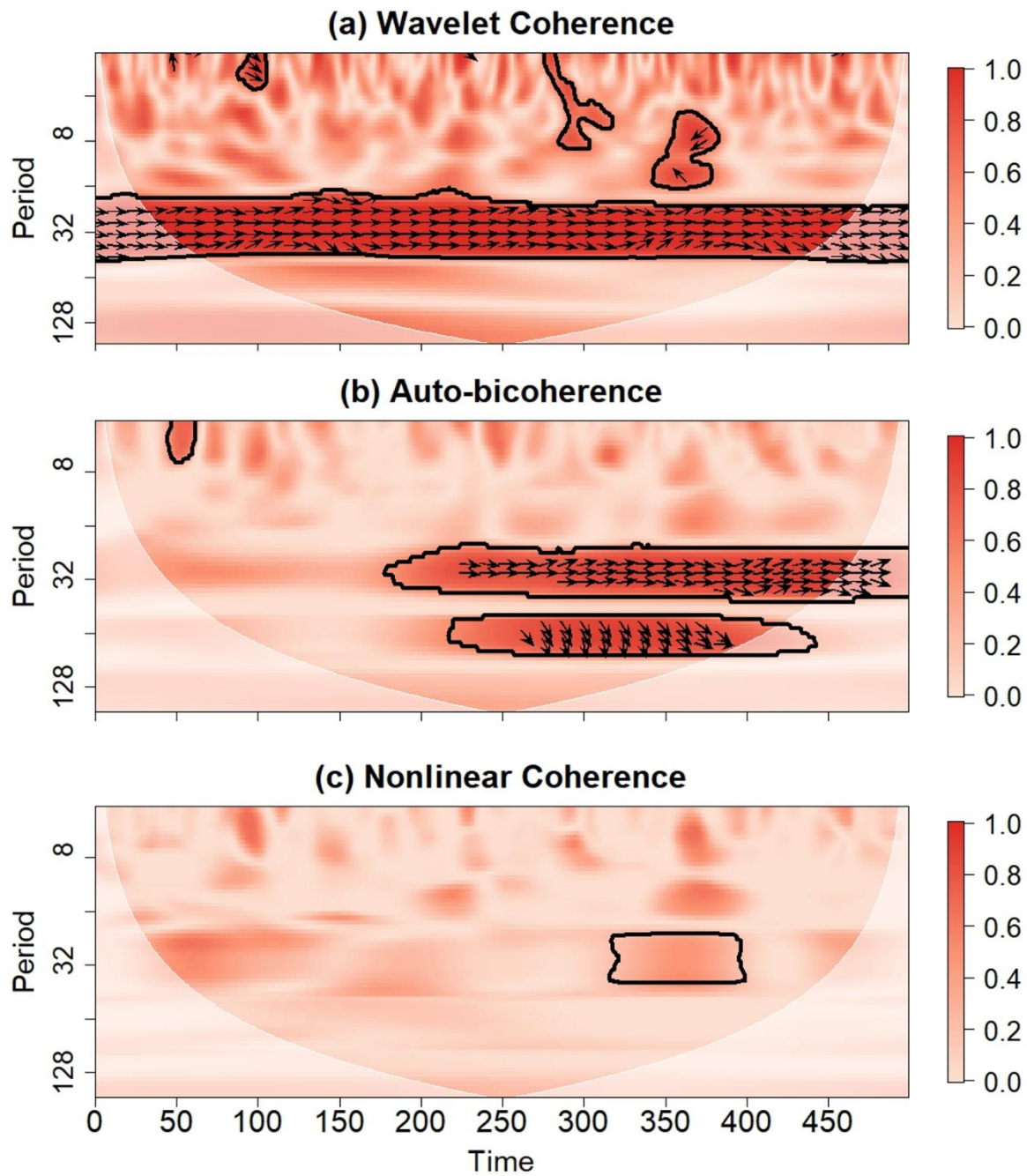
Figure 2. (a) Wavelet coherence between the time series of $F(t)$ and $R(t)$ shown in Figure 1. Arrows indicate the relative phase difference, where arrows pointing to the right mean that the time series are in phase. (b) The local diagonal slice of the auto-bicoherence spectrum of $F(t)$. Arrows represent the bi-phase, where arrows pointing to the right mean that the quadratic phase coupling between the mode with period indicated on the vertical axis and its harmonic contributes to positive skewness. (c) Nonlinear coherence between $F(t)$ and $R(t)$. Contours in all panels enclose regions of 5% cumulative area-wise significance. Light-shaded region represents the cone of influence where edge effects may be important.
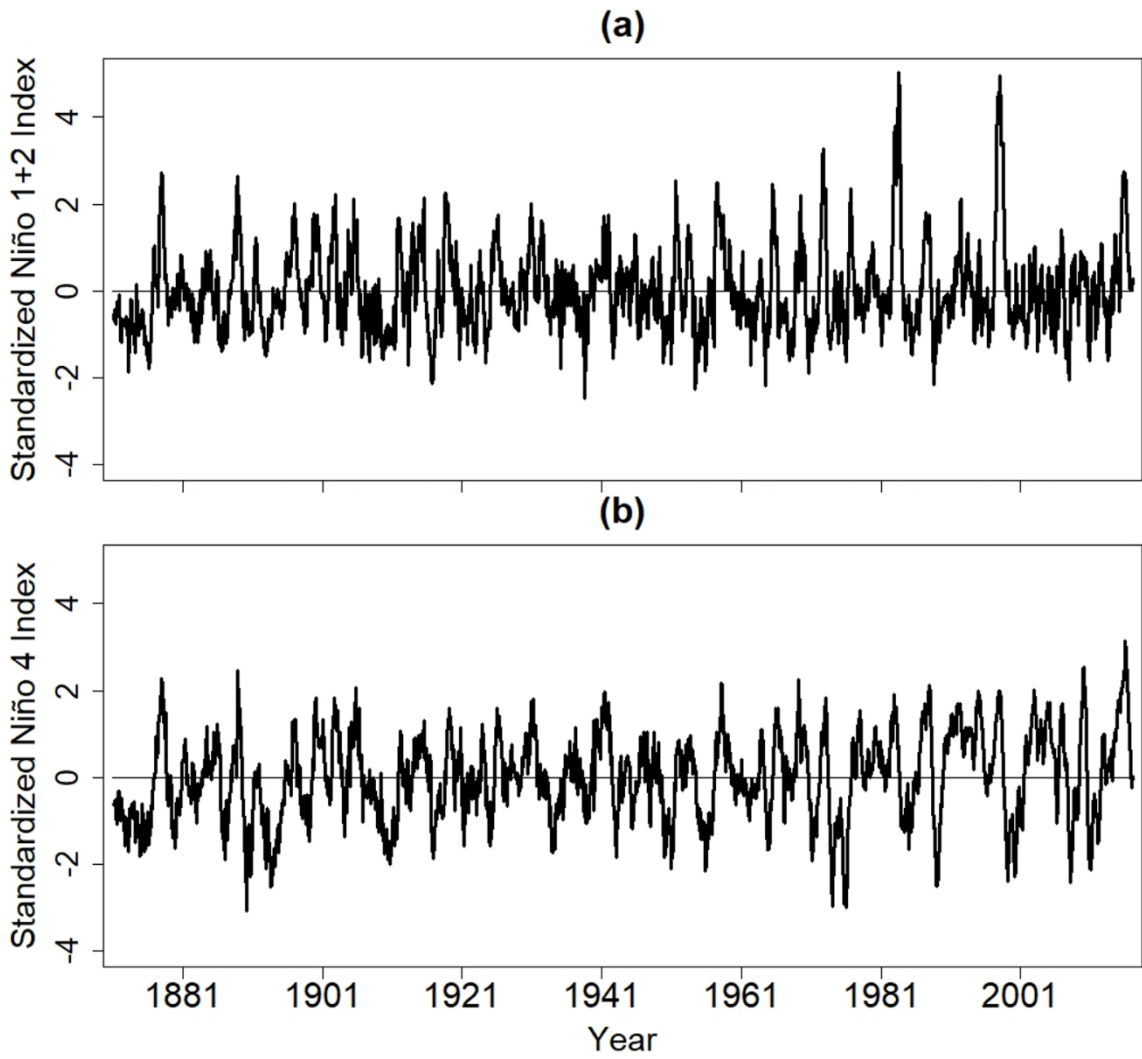
764

765 Figure 3. The time series of the (a) Niño 1+2 and (b) Niño 4 indices.
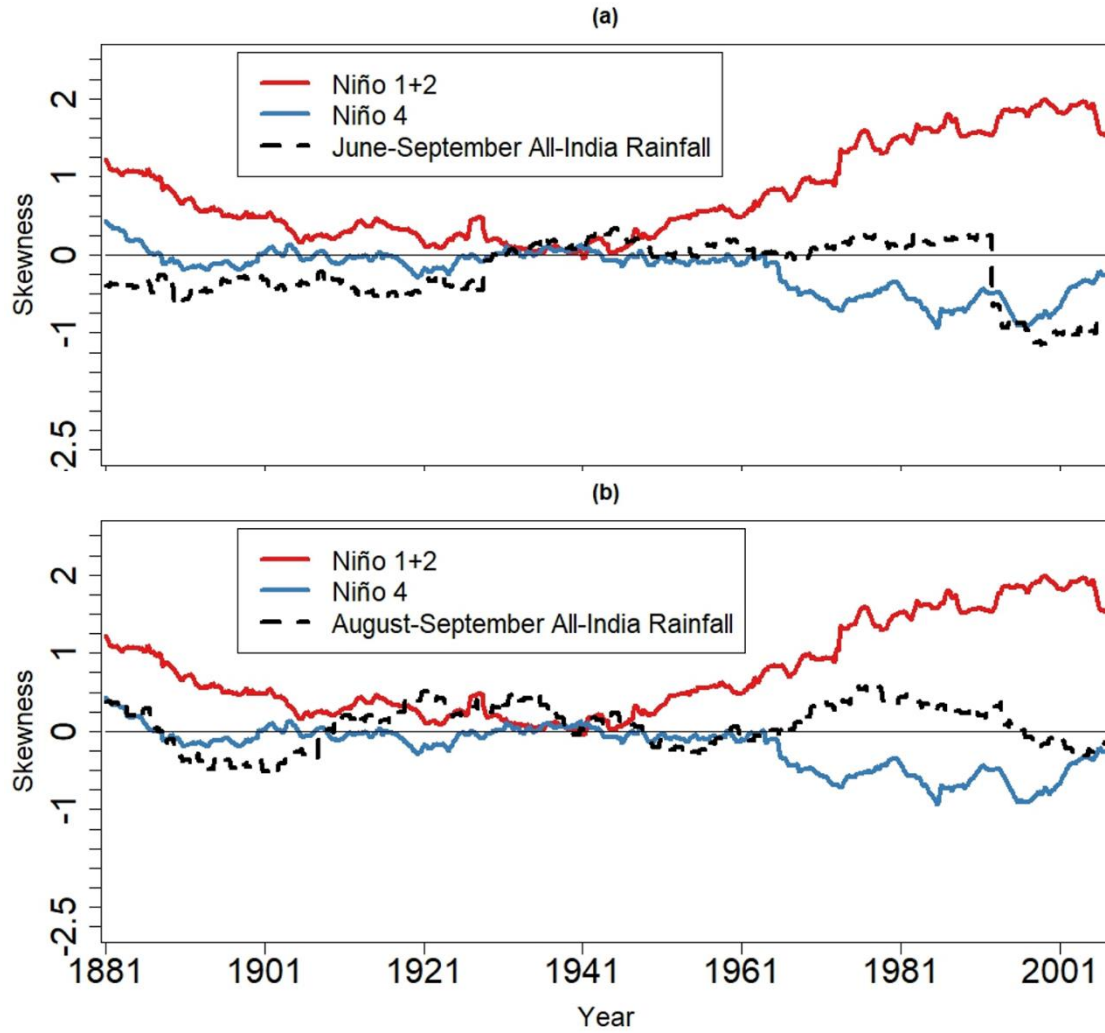
Figure 4. 20-year sliding skewness of (a) June-September and (b) August-September AIR and full time series for the Niño 1+2 and Niño 4 indices.

771
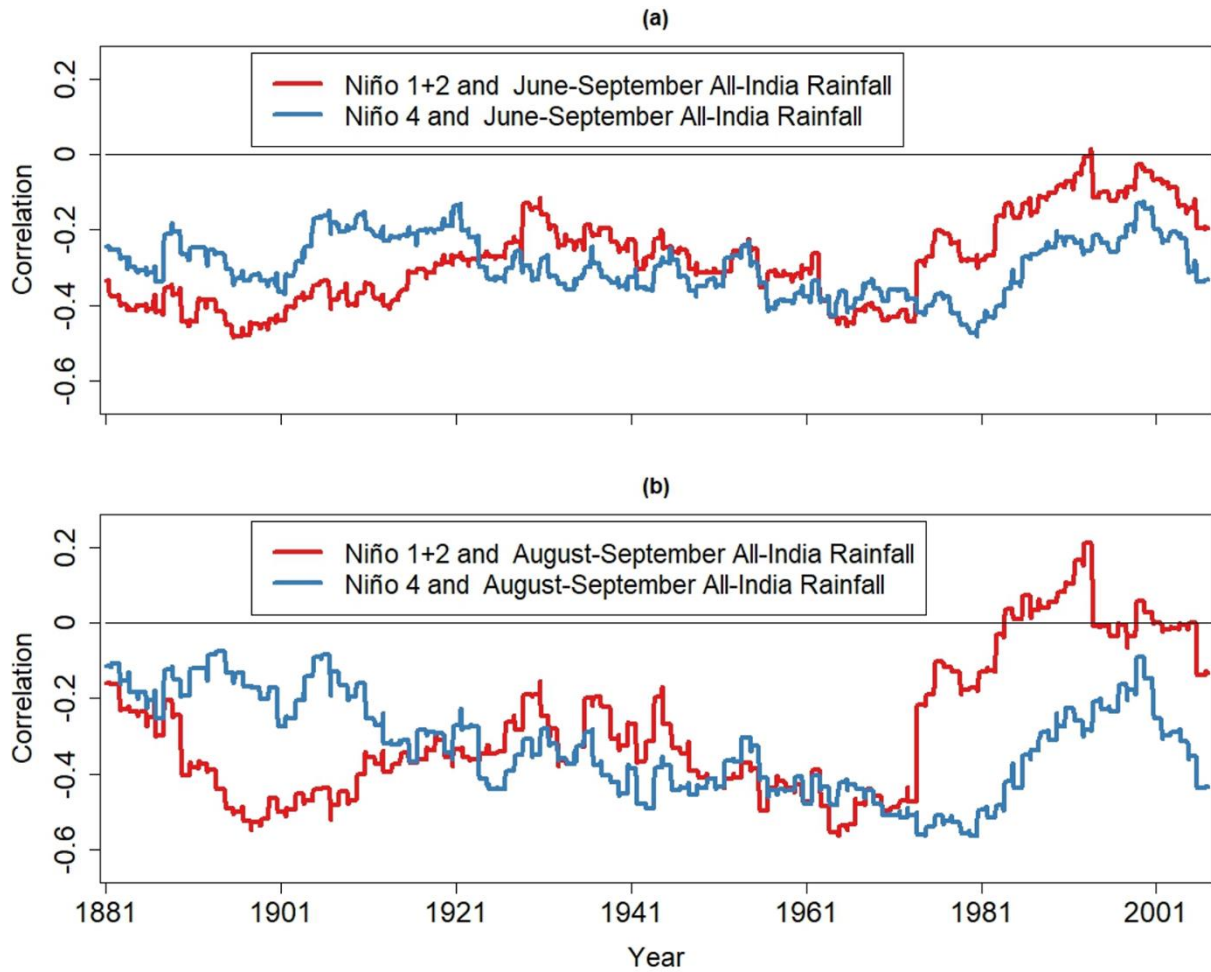
Figure 5. 20-year sliding correlation between anomalies for June-September AIR and the time series for the June-September Niño 1+2 and Niño 4 indices. (b) Same as (a) but for the August-September season.

774
775

776
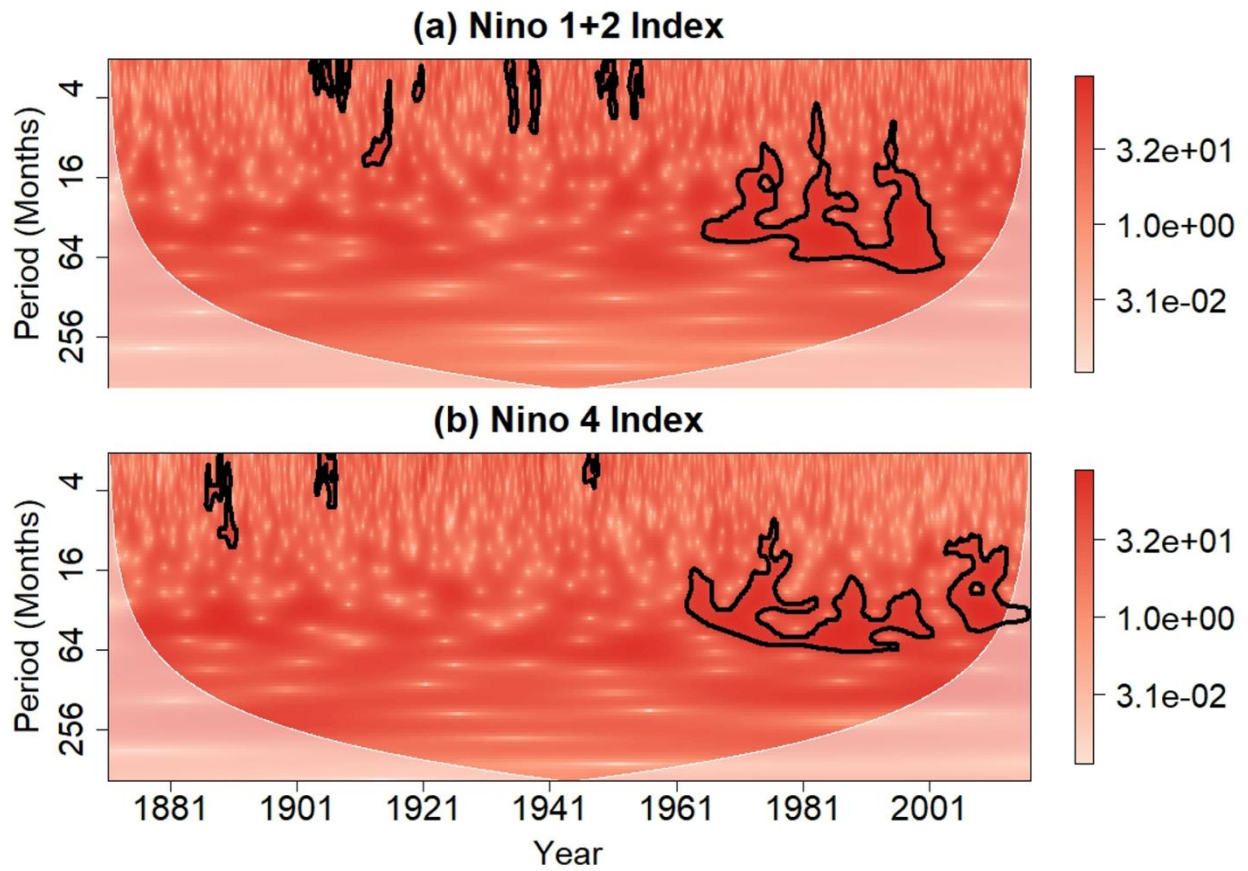
Figure 6. Wavelet Power spectrum of the (a) Niño 1+2 and (d) Niño 4 indices. Contours enclose regions of 5%
cumulative area-wise significance. Light-shaded region represents the cone of influence, which is the region where
edge effects are non-negligible.
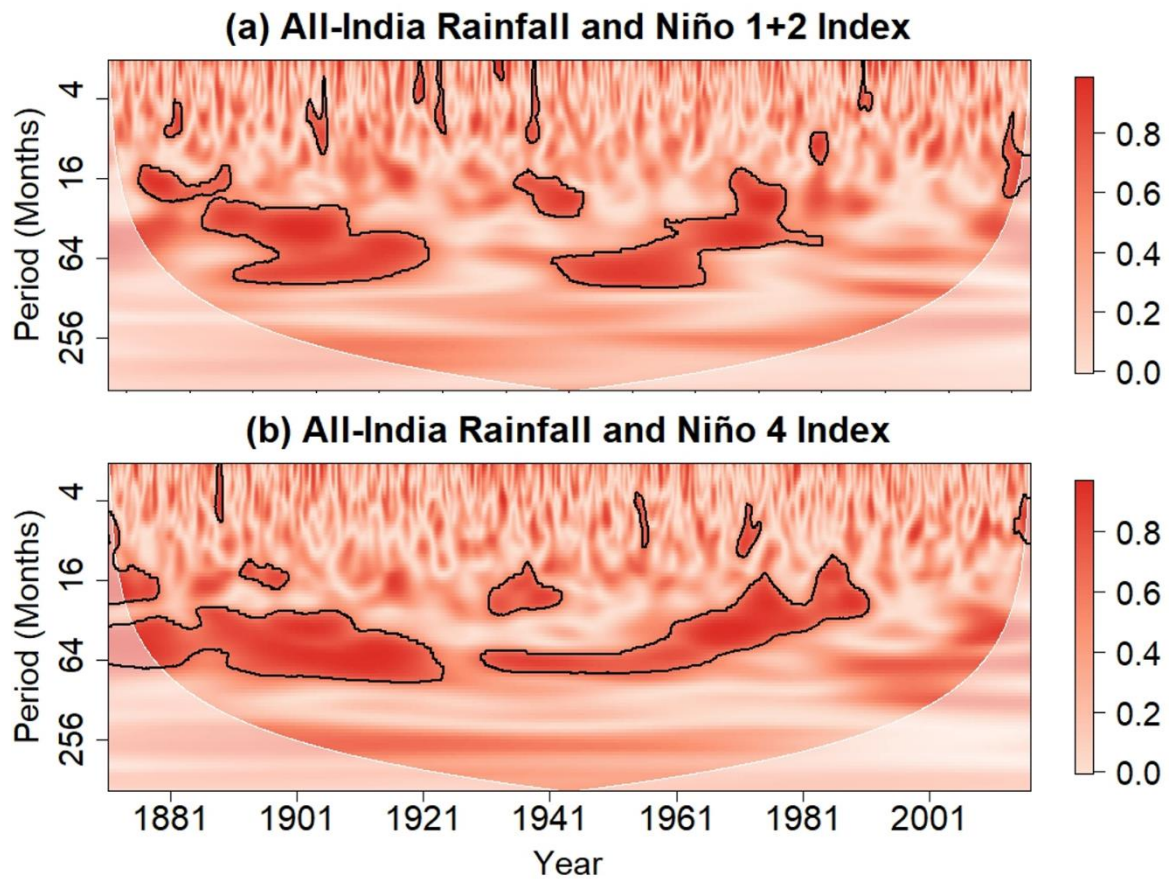
780
781 Figure 7. Wavelet coherence spectrum between AIR and time series for the (a) Niño 1+2 and (b) Niño 4 indices.
782 Contours enclose regions of 5% cumulative area-wise significance. Light-shaded region represents the cone of
783 influence, which is the region where edge effects are non-negligible.
784
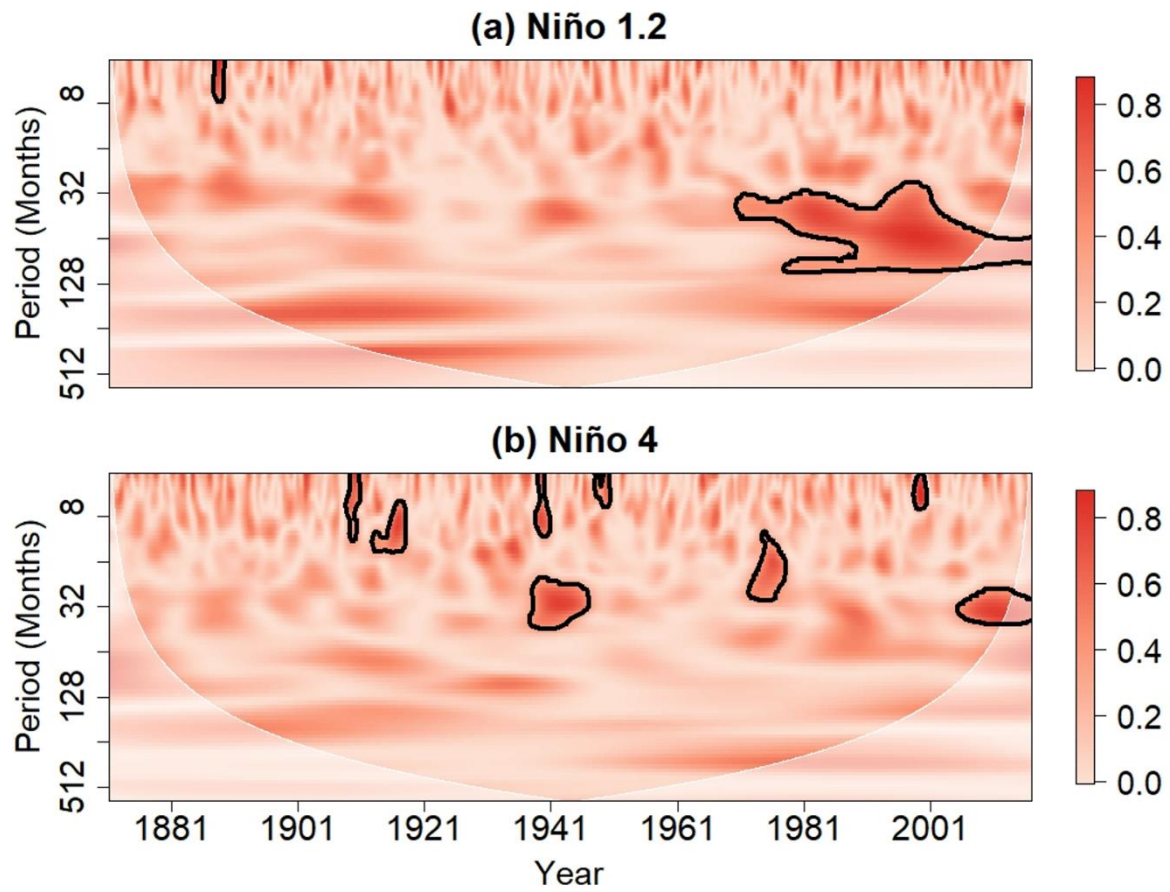
786
787 Figure 8. Local auto-bicoherence spectra of the (a) Niño 1+2 and (b) Niño 4 indices. Contours enclose regions of 5%
788 cumulative area-wise significance and the light shading represents the cone of influence.
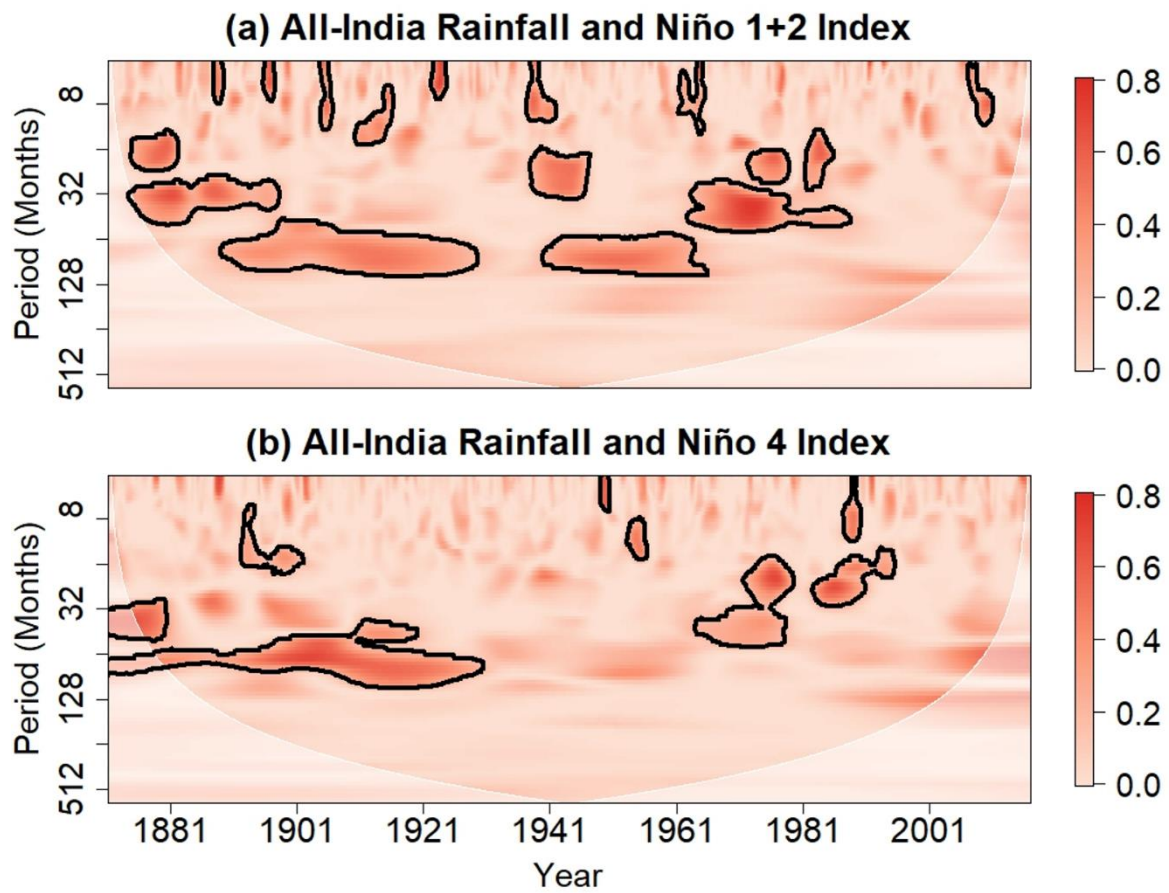
789
790 Figure 9. Nonlinear wavelet coherence between the full AIR time series and full times series for the (a) Niño 1+2 and
791 (b) Niño 4 indices. Contours enclose regions of 5% cumulative area-wise significance and light shading represents the
792 cone of influence.

793
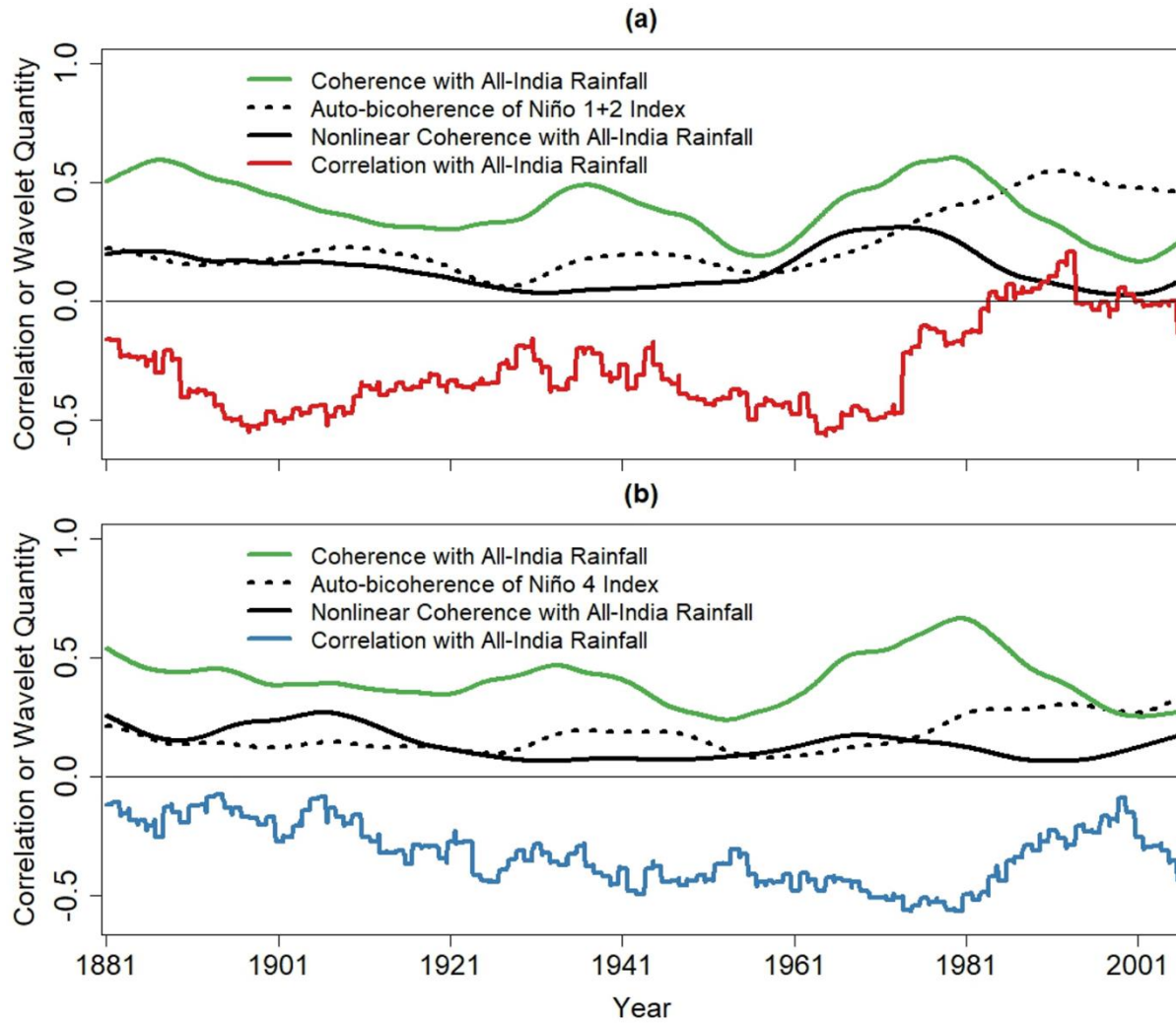
794
795 Figure 10. (a) 20-year sliding mean time series of the linear wavelet coherence between AIR and the Niño 1+ 2 index,
796 the auto-bicoherence of the Niño 1+2 index, and the nonlinear coherence between the Niño 1+2 index and AIR after
797 they have been averaged in the period band of 16 to 64 months. Red curve is the 20-year sliding correlation between
798 the August-September Niño 1+2 index and AIR. (b) The same as (a) but for the Niño 4 index. Blue curve is the 20-
799 year sliding correlation between the August-September Niño 4 Index and AIR.

800
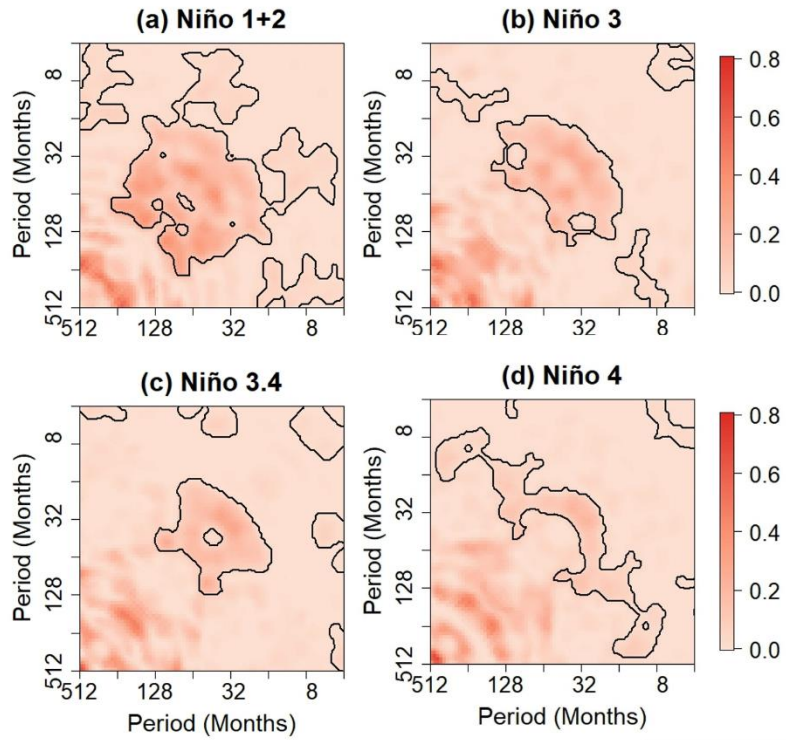
Figure 11. Global auto-bicoherence spectra of the (a) Niño 1+2, (b) Niño 3, (c) Niño 3.4, and (d) Niño 4 indices. Contours enclose regions of 5% cumulative area-wise significance.

807
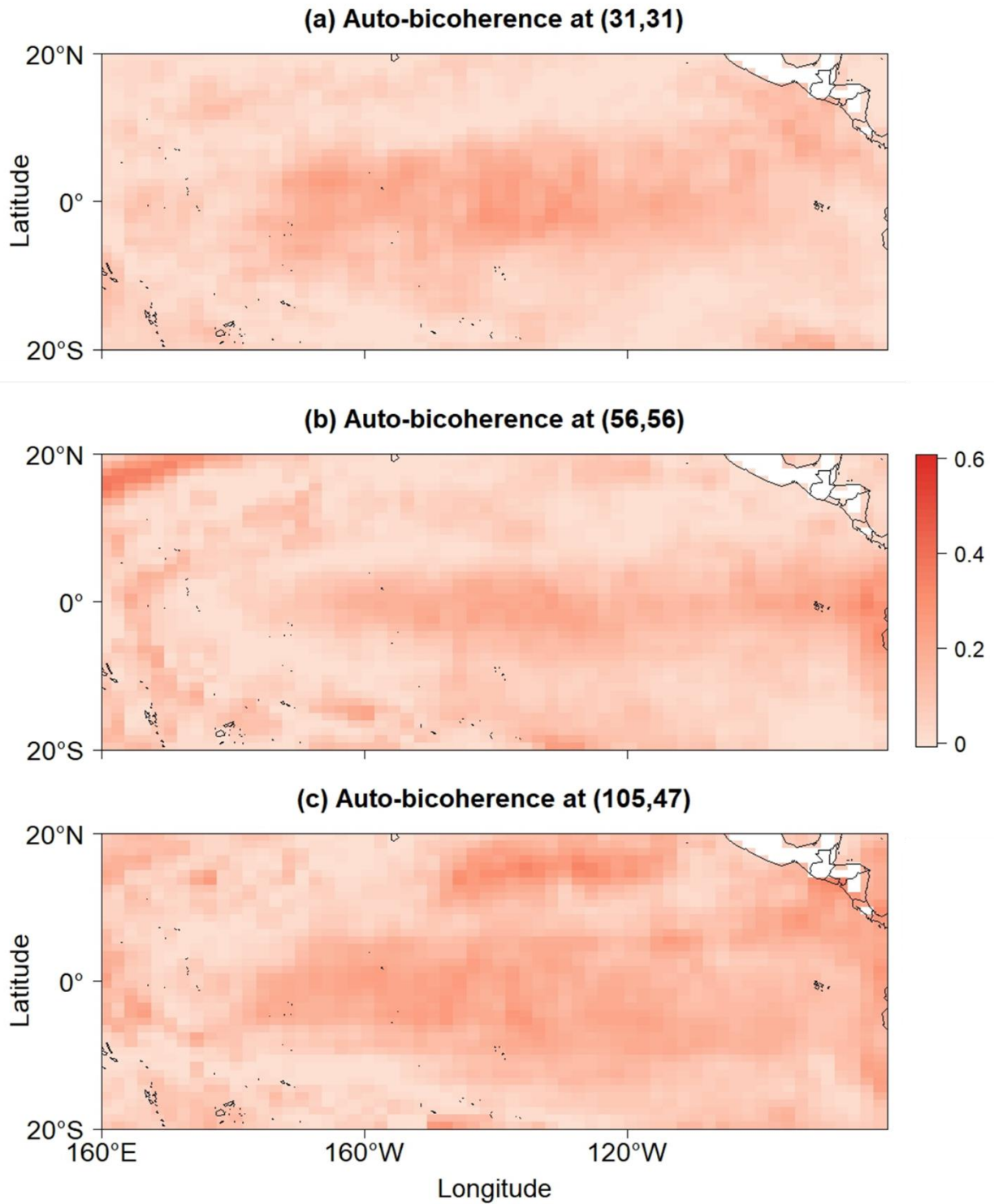
808

809   Figure 12. Global auto-bicoherence corresponding to the pairs (a) (31, 31), (b) (56, 56), and (c) (105, 47) [months].
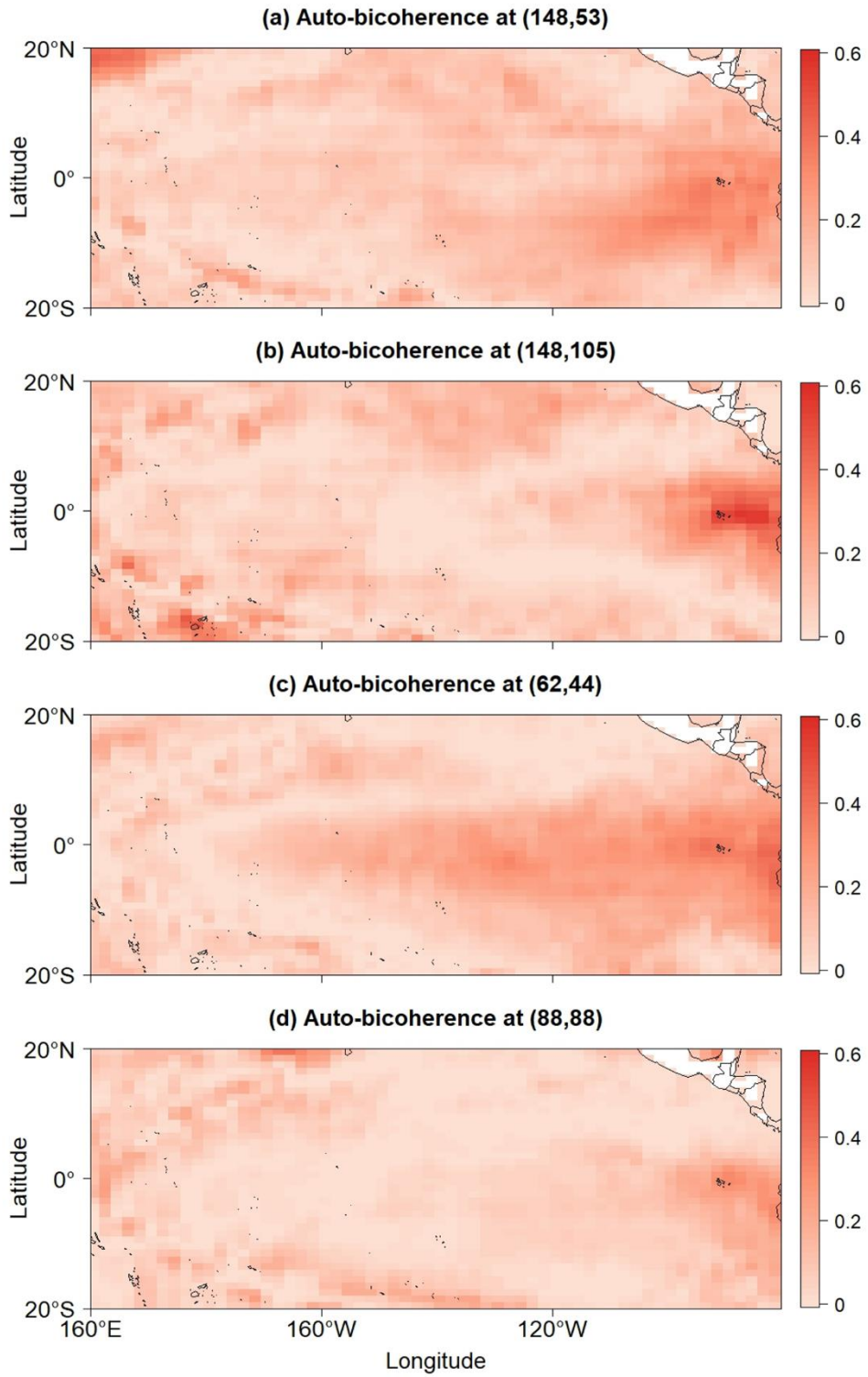
810

811   Figure 13. Global auto-bicoherence corresponding to the pairs (a) (158, 43), (b) (148, 105), (c) (62, 44), and (d)
812   (88,88) [months].

813

814   Table 1. Wavelet quantities and the relationships they measure.

Wavelet Quantity	Quantified Relationship
Linear Coherence	Cross-correlation between the variance of two time series at a Fourier period
Global Auto-bicoherence	Time-averaged quadratic phase coupling among two or three linear modes
Local Auto-bicoherence	Quadratic phase coupling among two or three linear modes at a time point
Nonlinear Coherence	Cross-correlation between the skewness of nonlinear modes

815

816

817

818